Mineralium Deposita

Stable H-C-O isotope and trace element geochemistry of the Cummins Range Carbonatite Complex, Kimberley region, Western Australia: Implications for hydrothermal REE mineralization, carbonatite evolution and mantle source regions
--Manuscript Draft--

Manuscript Number:	MIDE-D-14-00001R1
Full Title:	Stable H-C-O isotope and trace element geochemistry of the Cummins Range Carbonatite Complex, Kimberley region, Western Australia: Implications for hydrothermal REE mineralization, carbonatite evolution and mantle source regions
Article Type:	Regular Articles
Corresponding Author:	Peter Downes Western Australian Museum Welshpool DC, Western Australia AUSTRALIA
Corresponding Author Secondary Information:	
Corresponding Author's Institution:	Western Australian Museum
Corresponding Author's Secondary Institution:	
First Author:	Peter Downes
First Author Secondary Information:	
Order of Authors:	Peter Downes
	Attila Demény
	György Czuppon
	A. Lynton Jaques
	Michael Verrall
	Marcus Sweetapple
	David Adams
	Neal J McNaughton
	Lachland G Gwalani
	Brendan J Griffin
Order of Authors Secondary Information:	
Abstract:	The Neoproterozoic Cummins Range Carbonatite Complex (CRCC) is situated in the southern Halls Creek Orogen adjacent to the Kimberley Craton in northern Western Australia. The CRCC is a composite, sub-vertical to vertical stock ~2 km across with a rim of phlogopite-diopside clinopyroxenite surrounding a plug of calcite carbonatite and dolomite carbonatite dykes and veins that contain variable proportions of apatite-phlogopite-magnetite ± pyrochlore ± metasomatic Na-Ca amphiboles ± zircon. Early high-Sr calcite carbonatites (4800-6060 ppm Sr; La/YbCN = 31.6-41.5; δ13C = -4.2 to -4.0 ‰) possibly were derived from a carbonated silicate parental magma by fractional crystallization. Associated high-Sr dolomite carbonatites (4090-6310 ppm Sr; La/YbCN = 96.5-352) and a late-stage, narrow, high-REE dolomite carbonatite dyke (La/YbCN = 2756) define a shift in the C-O stable isotope data (δ18O = 7.5 to 12.6 ‰; δ13C = -4.2 to -2.2 ‰) from the primary carbonatite field that may have been produced by Rayleigh fractionation with magma crystallization and cooling, or through crustal contamination via fluid infiltration. Past exploration has focussed primarily on the secondary monazite-(Ce)-rich REE and U mineralization in the oxidised zone overlying the carbonatite. However, high-grade primary hydrothermal REE mineralization also occurs in narrow (<1 m wide) shear-zone hosted lenses of apatite-monazite-(Ce) and foliated monazite-(Ce)-talc rocks (≤~25.8 wt% TREO; La/YbCN = 30085), as well as in high-REE

	dolomite carbonatite dykes (3.43 wt% TREO), where calcite, parisite-(Ce) and synchysite-(Ce) replace monazite-(Ce) after apatite. Primary magmatic carbonatites were widely hydrothermally dolomitized to produce low-Sr dolomite carbonatite (38.5-282 ppm Sr; La/YbCN = 38.4-158.4; $\delta 18O$ = 20.8 to 21.9 ‰; $\delta 13C$ = -4.3 to -3.6 ‰) that contains weak REE mineralization in replacement textures, veins and coating vugs. The relatively high δD values (-54 to -34 ‰) of H_2O derived from carbonatites from the CRCC indicate that the fluids associated with carbonate formation contained a significant amount of crustal component in accordance with the elevated $\delta 13C$ values (~ -4 ‰). The high δD and $\delta 13C$ signature of the carbonatites may have been produced by CO_2-H_2O metasomatism of the mantle source during Paleoproterozoic subduction beneath the eastern margin of the Kimberley Craton.
Response to Reviewers:	See the attached file for a detailed response to reviewers comments.

1   **Stable H-C-O isotope and trace element geochemistry of the**

2   **Cummins Range Carbonatite Complex, Kimberley region,**

3   **Western Australia: Implications for hydrothermal REE**

4   **mineralization, carbonatite evolution and mantle source regions**

5

6   Peter J. Downes[1], Attila Demény[2], György Czuppon[2], A. Lynton Jaques[3], Michael Verrall[4],

7   Marcus Sweetapple[4], David Adams[5,6], Neal J. McNaughton[7], Lalchand G. Gwalani[8] and

8   Brendan J. Griffin[5]

9

10   [1]Department of Earth and Planetary Sciences, Western Australian Museum, Locked Bag

11   49, Welshpool DC, Western Australia, Australia. Email peter.downes@museum.wa.gov.au,

12   Ph: +61 8 92123757.

13   [2]Institute for Geological and Geochemical Research, Hungarian Academy of Sciences,

14   Hungary;

15   [3]Research School of Earth Sciences, Australian National University, Canberra, A.C.T.,

16   Australia;

17   [4]CSIRO Earth Science and Resource Engineering, Perth, Western Australia, Australia;

18   [5]Centre for Microscopy, Characterisation and Analysis, University of Western Australia,

19   Australia;

20   [6]GEMOC, Department of Earth and Planetary Sciences, Macquarie University,

21   NSW, Australia;

22 [7]John de Laeter Centre for Isotope Research, Curtin University, Western Australia,

23 Australia;

24 [8]Speewah Research Project C/- King River Copper Limited, B-26/122 Mounts Bay Road,

25 Perth, Western Australia, Australia

26

Abstract

28

29 The Neoproterozoic Cummins Range Carbonatite Complex (CRCC) is situated in the

30 southern Halls Creek Orogen adjacent to the Kimberley Craton in northern Western

31 Australia. The CRCC is a composite, sub-vertical to vertical stock ~2 km across with a rim

32 of phlogopite-diopside clinopyroxenite surrounding a plug of calcite carbonatite and

33 dolomite carbonatite dykes and veins that contain variable proportions of apatite–

34 phlogopite–magnetite ± pyrochlore ± metasomatic Na-Ca amphiboles ± zircon. Early high-

35 Sr calcite carbonatites (4800–6060 ppm Sr; La/Yb_{CN} = 31.6–41.5; $\delta^{13}C$ = -4.2 to -4.0 ‰)

36 possibly were derived from a carbonated silicate parental magma by fractional

37 crystallization. Associated high-Sr dolomite carbonatites (4090–6310 ppm Sr; La/Yb_{CN} =

38 96.5–352) and a late-stage, narrow, high-REE dolomite carbonatite dyke (La/Yb_{CN} = 2756)

39 define a shift in the C-O stable isotope data ($\delta^{18}O$ = 7.5 to 12.6 ‰; $\delta^{13}C$ = -4.2 to -2.2 ‰)

40 from the primary carbonatite field that may have been produced by Rayleigh fractionation

41 with magma crystallization and cooling, or through crustal contamination via fluid

42 infiltration. Past exploration has focussed primarily on the secondary monazite-(Ce)-rich

43 REE and U mineralization in the oxidised zone overlying the carbonatite. However, high-

grade primary hydrothermal REE mineralization also occurs in narrow (<1 m wide) shear-

zone hosted lenses of apatite-monazite-(Ce) and foliated monazite-(Ce)-talc rocks (≤~25.8

wt% TREO; La/Yb$_{CN}$ = 30085), as well as in high-REE dolomite carbonatite dykes (3.43

wt% TREO), where calcite, parisite-(Ce) and synchysite-(Ce) replace monazite-(Ce) after

apatite. Primary magmatic carbonatites were widely hydrothermally dolomitized to produce

low-Sr dolomite carbonatite (38.5–282 ppm Sr; La/Yb$_{CN}$ = 38.4–158.4; $\delta^{18}O$ = 20.8 to 21.9

‰; $\delta^{13}C$ = -4.3 to -3.6 ‰) that contains weak REE mineralization in replacement textures,

veins and coating vugs. The relatively high δD values (–54 to –34 ‰) of H_2O derived from

carbonatites from the CRCC indicate that the fluids associated with carbonate formation

contained a significant amount of crustal component in accordance with the elevated $\delta^{13}C$

values (~ -4 ‰). The high δD and $\delta^{13}C$ signature of the carbonatites may have been

produced by CO_2-H_2O metasomatism of the mantle source during Paleoproterozoic

subduction beneath the eastern margin of the Kimberley Craton.

Keywords

Carbonatite, REE mineralization, H-C-O stable isotopes, phoscorite, clinopyroxenite,

monazite-(Ce), Kimberley

Introduction

64   The Neoproterozoic Cummins Range Carbonatite Complex (CRCC) is situated at the

65   southern apex of the Halls Creek Orogen, close to its junction with the King Leopold

66   Orogen, adjacent to the Kimberley Craton in northern Western Australia (lat. 19º27'S, long.

67   127º10'E; Fig. 1). The CRCC is defined by a major magnetic anomaly and comprises a

68   composite, sub-vertical to vertical zoned stock in which a phlogopite-diopside

69   clinopyroxenite was intruded by calcite carbonatite and dolomite carbonatite dykes and

70   veins that contain variable proportions of apatite–phlogopite–magnetite ± pyrochlore ±

71   metasomatic Na-Ca amphiboles ± zircon (Fig. 2).

72   Past company exploration has focussed on the oxidised zone above the carbonatite

73   which contains a REE ore body with an inferred resource of 4.90 Mt at 1.74% TREO,

74   11.2% P_2O_5 and 145 ppm U_3O_8 (Kimberley Rare Earths 2012). This monazite-(Ce)-apatite-

75   rich secondary ore largely formed through the mechanical concentration of primary

76   magmatic–hydrothermal REE mineralization within the carbonatite during weathering and

77   deflation. The ore body is the third largest REE resource in Western Australia behind the

78   Mt Weld deposit and the Hastings-Brockman trachytic tuff (Geological Survey of Western

79   Australia 2011).

80   In this paper we employ H-C-O stable isotope and whole-rock geochemistry to define

81   the evolution of various phases of the Cummins Range carbonatite and associated

82   hydrothermal–metasomatic processes involved in REE mineralization. H-C-O isotope data

83   also provides information on the development of the mantle source regions for the CRCC

84   where previous work has indicated the influence of subduction-related processes and the

85   existence of a Neoarchean depleted lithospheric mantle root beneath the Halls Creek

86   Orogen (Jaques et al. 1989a; Luguet et al. 2009; Honda et al. 2012).

87

Geological setting

89

90 The Paleoproterozoic Halls Creek Orogen is comprised of a NNE-trending band of

91 deformed and metamorphosed sedimentary, volcanic and intrusive rocks that represents a

92 suture zone between the Kimberley Craton and the remainder of the North Australian

93 Craton to the east (Fig. 1). Amalgamation following plate collision had occurred by ~1820

94 Ma (Myers et al. 1996; Tyler et al. 1999; 2012; Griffin et al. 2000; Cawood and Korsch

95 2008; Richards 2013). The Argyle lamproite, associated lamproite dykes and the Bow Hill

96 ultramafic lamprophyre dykes were emplaced along a terrane boundary within the Halls

97 Creek Orogen during the Proterozoic (Fig. 1; Jaques et al. 1986; Jaques and Milligan 2004).

98 Similarly, a deep crustal structure within the King Leopold Orogen probably provided a

99 route for lamproite magmas to reach the surface during the Miocene (~17–22 Ma)

100 volcanism in the West Kimberley (Ellendale; Fig. 1; Jaques and Milligan 2004). The

101 Cummins Range Carbonatite Complex has been interpreted by a number of workers to be

102 emplaced in the proximity of the Halls Creek Fault (Fig. 1; e.g. Sanders 1999). Country

103 rocks, including granite gneiss and chlorite schist, are interpreted to be part of the Eastern

104 zone of the Paleoproterozoic Lamboo Complex within the Halls Creek Orogen (Fig. 2;

105 Andrew 1990; cf. Hassan 2000). The contacts of the CRCC are largely inferred from

106 magnetic data and no structural disruption or contact metamorphism was found on the

107 margins of the carbonatite complex. Neoproterozoic ages of ~854–1012 Ma (currently

108 under review) are indicated for the CRCC by dating using various methods (Pidgeon et al.

109 1986; Sun et al. 1986).

110

111   Outline of Geology

112

113   Previous detailed accounts of the geology and mineralogy of the intrusive complex may be

114   found in Richards (1983, 1985) and Andrew (1990). The CRCC has little surface

115   expression, with the area largely being concealed by an aeolian sand sheet of varying

116   thickness, typical of the Great Sandy Desert. Exposure is limited to patchy outcrop of low

117   mounds of jasperoidal matrix-supported ironstone breccia, interpreted to be a residual

118   solution collapse breccia of karst origin (Fig. 2; Richards 1983). Other regolith units noted

119   within, or beneath sand cover, are ferruginous laterite, silcrete and calcrete. Resistate

120   minerals, including REE-bearing monazite-(Ce), apatite, zircon and pyrochlore are

121   considered to have been enriched by up to 10 times their original concentration in the

122   oxidised zone (Andrew 1990), but the nature of this enrichment is not well defined.

123   Drilling and aeromagnetic and more detailed ground magnetic surveys have shown that

124   the CRCC is a composite, sub-vertical to vertical stock some 1.8 x 1.6 km in maximum

125   dimensions with three broadly concentric zones (Fig. 2). A central intrusive zone or plug

126   of calcite carbonatite and dolomite carbonatite dykes is surrounded by variably carbonated

127   and metasomatically altered phlogopite clinopyroxenite. Adjacent to the central carbonatite

128   intrusive zone the clinopyroxenite was intruded by numerous steeply-dipping carbonatite

129   dykes up to ~60m thick and metasomatism of the clinopyroxenite by the carbonatite is most

130   intense in this zone, where there is a high density of carbonate veins/microveins and

131   invasion of the clinopyroxenite by carbonatite (Andrew 1990). The outer envelope

132   comprises less altered clinopyroxenite with a mineral assemblage that includes phlogopite,

133   diopside, apatite, magnetite, calcite and ilmenite, and lesser amounts of metasomatic Na-Ca

134   amphiboles and accessory zirconolite (Table 1; Fig. 2). Sulfide ± oxide assemblages

135   composed of pyrrhotite, pyrite, chalcopyrite, ± sphalerite ± galena ± magnetite are common

136   to both the clinopyroxenite and various phases of the carbonatite, where they may form

137   sulfide-rich bands and lenses. Within the carbonatite, vugs up to several centimetres wide

138   commonly contain hydrothermal pyrite, marcasite and chalcopyrite (Table 1). Sulfides

139   exhibit textures that suggest that they have formed through the replacement of carbonates

140   (calcite and dolomite), diopside (or actinolite), to a lesser extent apatite, and rarely

141   monazite-(Ce).

142   The carbonatite and clinopyroxenite are cut by vertical–sub vertical shear zones,

143   trending ~315–330˚, that include weakly to strongly foliated dolomite carbonatite, zones of

144   phlogopitite, and zones of high-REE apatite-monazite-(Ce) rock (Fig. 3). Some shear zones

145   have been localised along contacts between the clinopyroxenite and carbonatite and this

146   deformation may have played a major role in producing foliated phlogopitite along the

147   margins of some clinopyroxenite bodies. This apparent K-metasomatism does not appear to

148   have been entirely related to contact metasomatism with the intrusion

149   of carbonatite into clinopyroxenite, because zones of phlogopitite are asymmetric in

150   distribution. At some boundaries of the clinopyroxenite there are quite thick zones

151   of phlogopitite (≤~10 m), but at others minimal phlogopitite is developed (cm-scale). This

152   suggests a correlation with zones of shearing. The shear zone trend of ~315–330˚ may also

153   be reflected in the approximate orientation of the outcrop of iron oxide collapse breccias

154   (Fig. 2) and the orientation of the REE orebody within the oxidised zone (see Appendix 1).

155

Analytical methods

156

157

158   Scanning electron microscopy and electron microprobe microanalysis

159

160   Mineral identifications were assisted by detailed back-scattered electron (BSE) imaging and

161   energy-dispersive X-ray spectrometry (EDS) using a Philips XL-40 scanning-electron

162   microscope (SEM) at CSIRO Earth Science and Resource Engineering, Perth.

163   The composition of apatite was determine at the Centre for Microscopy,

164   Characterisation and Analysis at the University of Western Australia using a field emission

165   gun JEOL JXA-8530F Hyperprobe with five wavelength-dispersive spectrometers

166   operating at 20 keV, 50 nA, and a 10 μm diameter beam to minimise fluorine diffusion. All

167   analyses were performed using the Probe for EMPA software by Probe Software, Inc. F and

168   Ca were analysed first using a Time Dependent Intensity (TDI) correction to account for

169   any anisotropic elemental diffusion during analysis. REEs were standardised using the

170   Smithsonian Institution single element orthophosphate standards. Ca and F were

171   standardised on Durango apatite; Cl was standardised on a Brazilian sodalite. Natural

172   orthoclase was used as the standard for Si and K, and San Carlos olivine was used for Fe

173   calibration. Sr was calibrated on synthetic celestine and synthetic barite was used for S.

174   Standards used for U, Th, and Pb were U metal, ThO_2, and crocoite respectively. All REEs,

175   Th, and U were counted for 100 seconds on peak and major elements were counted for 10 –

176   40 seconds on peak. All elemental peak overlaps were accounted for and eliminated using

177   software peak overlap correction routines. Errors on all elements are $\leq 10\%$.

178

179 Whole-rock geochemistry

180

181 Abundances of major and trace elements were determined at Geoscience Australia,

182 Canberra by XRF and ICP-MS for selected samples. Major and minor elements (Si, Ti, Al,

183 Fe, Mn, Mg, Ca, Na, K, P and S) were determined by wavelength-dispersive (Bruker

184 S8Tiger) XRF on fused disks using methods similar to those of Norrish and Hutton

185 (1969). Precision for these elements is better than ±1% of the reported values. As, Ba, Cr,

186 Cu, Ni, Sc, V, Zn, Zr, F and Cl were determined by XRF on pressed pellets using methods

187 similar to those described by Norrish and Chappell (1977). Loss on Ignition (LOI) was by

188 gravimetry after combustion at 1100°C. FeO abundances were determined by digestion and

189 electrochemical titration using a modified methodology based on Shapiro and Brannock

190 (1962), and Fe_2O_3 values were calculated as the difference between total Fe, determined by

191 XRF, and FeO. Selected trace elements (Cs, Ga, Nb, Pb, Rb, Sb, Sn, Sr, Ta, Th, U, Y) and

192 the Rare Earth elements were analysed by ICP-MS (Agilent 7500 with reaction cell) using

193 methods similar to those of Eggins et al. (1997), but on solutions obtained by dissolution of

194 fused glass disks (Pyke 2000). Precisions are ±5% and ±10% at low levels (<20 ppm).

195 Agreement between XRF and ICP-MS are typically within 10%. Because of problems in

196 retaining the sample in solution, the REE and F-rich fused XRF disc of sample CDD1-36

197 (and CDD1-34 for comparison) was also analysed by laser ablation ICP-MS at the

198 Research School of Earth Sciences, ANU, for REEs and other trace elements using an

199 Agilent Technologies 7700 ICP-MS coupled to an ANU HelEX laser-ablation system with

200 a 193 nm wavelength EXCIMER laser (110 (ArF) COMPex, Lambda Physik) following the

201   method of Jenner and O'Neill (2012). Data acquisition involved a 20 second background

202   measurement followed by 45 seconds of ablation, employing an 81 micron diameter laser

203   spot, 5 Hz repetition rate and 50-55 mJ fluence. Samples were analysed by bracketing every

204   5 unknowns with analyses of NIST610 and BCR2G reference glasses. Data were processed

205   using the Iolite software package (Paton et al. 2011). Agreement of the LA-ICP-MS and

206   solution ICP-MS methods for sample CDD1-34, and with recommended/preferred values

207   for standards BCR-2G and SY-3 was within 10% for most elements at the ppm level and

208   higher. LA-ICP-MS data for the REEs, Zr, Hf, Ta, Th and U in sample CDD1-36, and Tm,

209   Hf and Ta in sample CDD1-34, are therefore reported here.

210   Abundances of trace elements for 9 rock samples were determined at TSW Analytical,

211   Perth (analyst Sven Fjastad) using a combination of ICP-MS (Agilent 7700) and ICP-AES

212   (Thermo Scientific iCAP) analysis. Solutions for analysis were prepared by two methods:

213   (a) The pulverised sample (0.3 g) was fused with lithium tetraborate (35.3%)/lithium

214   metaborate (64.7%) flux (0.8 g) at 1050°C for 15 minutes, then the fused material was

215   dissolved in a citric acid solution (50 mL, 10% m/v); and (b) The pulverised sample (0.25

216   g) was digested in a mixture of nitric, perchloric and hydrofluoric acids. The digestate was

217   taken to incipient dryness and the residue dissolved in a mixture of nitric and hydrochloric

218   acid then diluted with ultra-pure water to produce a final acid strength of ~5% v/v. The

219   resultant solutions were then diluted appropriately for ICP-AES and ICP-MS analysis.

220   The elements reported for these samples have been compiled from, and confirmed by,

221   using both the ICP-AES and ICP-MS results from the above sample preparation techniques.

222   The detection limits vary from element to element in the various solution matrices and

223   instrumental technique used, however as a generalisation elements reported from the ICP-

224 AES assay have limits of detection (2σ) of approximately 10 ppm in the pulverised sample

225 and elements reported from the ICP-MS assay have limits of detection (2σ) of

226 approximately 0.1 ppm in the pulverised sample.

227

228 Stable Isotopes

229

230 For carbonate samples from the CRCC the stable carbon and oxygen isotope compositions

231 were determined by applying the carbonate-orthophosphoric acid reaction at 72ºC (Spötl

232 and Wennemann 2003) and using an automated GASBENCH II sample preparation device

233 attached to a Thermo Finnigan Delta Plus XP mass spectrometer at the Institute for

234 Geological and Geochemical Research, Budapest, Hungary.

235 Hydrogen isotope compositions of fluid inclusion-hosted H_2O and H_2O-contents in

236 ten carbonate samples were determined by vacuum-crushing followed by H_2O purification

237 by vacuum distillation, reaction with Zn at 480ºC to produce H_2 gas and mass spectrometric

238 analyses of D/H ratios (see Demény 1995, Demény and Siklósy 2008, Czuppon et al. 2014)

239 using a Finnigan MAT delta S mass spectrometer at the Institute for Geological and

240 Geochemical Research.

241 The isotope compositions are given as δD, $δ^{13}C$ and $δ^{18}O$ in parts per thousands (‰)

242 relative to V-PDB ($δ^{13}C$) and V-SMOW (δD and $δ^{18}O$), according to the equation: δ =

243 (Rsample/Rstandard–1) × 1000, where R is the D/H, $^{13}C/^{12}C$ or $^{18}O/^{16}O$ ratio in the sample

244 or in the international standard. The measurement precision is better than 0.15‰ for C and

245 O isotope data based on replicate measurements of international standards (NBS-19; NBS-

246   18) and in–house reference materials. Reproducibilities of H isotope analyses were about

247   3‰ for δD values based on duplicate analyses.

248   Two samples of the high-REE apatite-monazite-(Ce) rock (CDD1-31, CDD1-37A)

249   were examined and found not to contain fluid inclusions.

250

Petrography

251

252

253   Fresh rocks within the Cummins Range complex were encountered in two deep inclined

254   diamond drill holes, CDD1 and CDD2, each ~402 m long (Figs 2, 3; Appendix 1). The

255   petrographic descriptions presented here are based mostly on samples from these drill

256   holes. Most exploration drilling has concentrated on defining the shallow REE resource

257   within the oxidised zone. Two of the samples analysed for C-O isotopes came from shallow

258   RC drill holes (NRC035 92–93 m, NRC058 97–98 m). We describe the various

259   carbonatites and the high-REE apatite-monazite-(Ce) rock in detail here, but the associated

260   clinopyroxenite will be described elsewhere (Table 1).

261   We use the term 'phoscorite' to describe apatite-amphibole-rich rocks that also contain

262   varying proportions of phlogopite, magnetite, dolomite, ± calcite ± ilmenite (Table 1). No

263   olivine-bearing rocks have been found in the CRCC. The definition of 'phoscorite' or

264   'phoscorite-series' rocks is complex, and this is discussed in detail by Krasnova et al.

265   (2004).

266

267   Carbonatites

268

269   Multiple phases of calcite carbonatite and dolomite carbonatite dykes intruded the

270   clinopyroxenite phase of the CRCC producing a central carbonatite plug (Fig. 2). The

271   carbonatites contain variable proportions of apatite ± phlogopite ± magnetite ± amphibole,

272   and with increasing content of these minerals range towards silicocarbonatites or

273   phoscorite-series rocks (Table 1; Fig. 4). Blue-green, Na-Ca amphiboles (predominantly

274   richterite) are a metasomatic phase (≤~5 vol.%) that overprint the magmatic carbonatite

275   rock fabric, including replacement of phlogopite and apatite (Fig. 4b, c). Contact

276   relationships between carbonatites and associated phoscorite-series rocks commonly are

277   gradational. Fresh diopside has not been observed in the carbonatites at Cummins Range,

278   however diopside may have been a primary magmatic phase that has been replaced by

279   richterite in associated apatite-amphibole-rich phoscorite.

280   The carbonatites vary from fine to coarse-grained, and from massive to foliated. The

281   foliated textures indicate ductile deformation of the carbonatite during tectonism (Fig. 4d).

282   Generally, the carbonatites are either calcite or dolomite dominant, where the carbonates

283   comprise up to ~95 vol.% of the rock. Recrystallization and hydrothermal alteration of the

284   carbonatites has produced massive, turbid, microporous dolomite or calcite in some zones.

285   In the carbonatites, apatite occurs as individual equant to elongate crystals (≤1.5 cm long)

286   or as radiating to divergent clusters of elongate crystals (≤4 cm across) generally situated at

287   calcite or dolomite grain boundaries, or in lenses of polygonal crystal cumulate (Fig. 4c).

288   Pyrochlore and zircon are characteristic minor accessory minerals. Pyrochlore (generally

289   <1 vol.%) occurs as equant, euhedral to anhedral, dark brown to golden brown crystals

290 ≤10mm wide. It is commonly overgrown by thin rims of pyrite, and very rarely is replaced

291 by ferrocolumbite. Zircon exhibits a diverse range of textures including subhedral

292 megacrysts to ~1.5cm wide with typical igneous growth zonation (Fig. 4a; occurring in

293 CDD1 323–331 m), anhedral, metamict composite porphyroblasts intergrown with

294 dolomite in strongly foliated carbonatite (≤3 mm wide; Fig. 4d), and turbid brown

295 anhedral–subhedral crystals intergrown with amphibole-ilmenite-apatite-dolomite (≤5 mm

296 wide). Textural relationships indicate that the zircon is variably igneous to hydrothermal or

297 metasomatic in origin. The zircons have a very low U content (≤138 ppm; unpubl. data NJ

298 McNaughton) consistent with their carbonatite origin (cf. Belousova et al. 2002).

299   Carbonatites within the CRCC commonly contain trace–minor hydrothermal REE-

300 mineralization (generally <1 vol.%) in the form of disseminated grains of monazite-(Ce),

301 parisite-(Ce) and synchysite-(Ce) in calcite and dolomite; monazite-(Ce) rimming and

302 replacing magmatic apatite; parisite-(Ce) and synchysite-(Ce) in replacement textures,

303 veins and lining cavities in carbonatite; as well as minor nioboaeschynite-(Ce), chevkinite-

304 (Ce), fergusonite and Ca-REE-Ba-Sr carbonates (possibly burbankite or carbocernaite; Fig.

305 5).

306

307 *High-Sr calcite carbonatite*

308

309 Calcite carbonatites may have a fine-grained, equigranular to inequigranular polygonal

310 mosaic texture (with straight to slightly curved grain boundaries; crystals ≤1 mm wide), but

311 vary to inequigranular textures where carbonate crystals (≤5 mm long) have irregular to

312   serrated boundaries. White–light grey, massive carbonatite may be intruded (and/or

313   replaced?) by dykes or irregular bodies of light pink calcite carbonatite that occurs only in

314   the drill hole CDD1 (Fig. 4a). This calcite carbonatite may contain minor subhedral to

315   anhedral, phenocrysts and crystal clusters of white dolomite (≤~5 mm long; <15 vol.%) in a

316   calcite groundmass (Fig. 4a). High-Sr calcite carbonatite near the bottom of drill hole

317   CDD2 preserves calcite-dolomite exsolution textures. Small blebs and rods of dolomite

318   (≤~20 μm long) have exsolved from high-Mg calcite.

319

320   *High-Sr dolomite carbonatite*

321

322   White, massive, weakly–moderately fractured dolomite carbonatite is present in both drill

323   holes (e.g. CDD1 150.45–152.26 m; CDD2 ~110–115 m). Generally, it has indistinct

324   contacts with surrounding calcite carbonatite, but is intruded by pink high-Sr calcite

325   carbonatite. The texture varies from zones of inequigranular, variably clear to turbid

326   dolomite, with crystals up to ~2 mm wide having straight to curved or rounded boundaries,

327   grading into a more coarse-grained turbid dolomite with elongated–anhedral crystals

328   ≤~1.25 cm long. This dolomite carbonatite contains rare parisite-(Ce), synchysite-(Ce) and

329   monazite-(Ce) (<1 vol.%). Minor patches and crystals of calcite exhibit microporosity and

330   contain inclusions of strontianite and Ca-REE-Ba-Sr minerals (possibly burbankite or

331   carbocernaite; ≤30 μm long).

332

333   *High-REE dolomite carbonatite dykes*

334

335   Late-stage, thin, grey dolomite carbonatite dykes intrude calcite and calcite-dolomite

336   carbonatite over two intervals within the drill hole CDD2. These dykes contain relatively

337   high-grade REE mineralization (e.g. CDD2 396.9–397.64 m – 3.43 wt% TREO) and their

338   texture and mineralogy are as follows:

339   1) The grey, medium-grained dolomite carbonatite dyke intruding calcite-dolomite

340   carbonatite over the interval CDD2 225.03–225.23 m, contains turbid dolomite and

341   parisite-(Ce) (~15–20 vol.%; elongate crystals ≤3 mm) with minor aeschynite-(Ce)

342   (crystals ≤~0.8 mm long), monazite-(Ce) and pyrite (Fig. 5a, b). Crystals of parisite-

343   (Ce) are partially resorbed or altered and fractured, with dissolution along cleavage

344   planes. Pyrite (crystals ≤~0.6 mm long) commonly occurs along fractures and cleavage

345   planes in crystals of parisite-(Ce).

346   2) Dolomite carbonatite dykes intrude calcite carbonatite over the interval CDD2 396.9–

347   397.18 m, 397.35–397.64 m. The REE mineralization in these dykes comprises fine-

348   grained monazite-(Ce), parisite-(Ce) and synchysite-(Ce) in irregularly-shaped patches

349   of pink calcite up to 2 cm long (Fig. 5c, d). Crystals of apatite may be partially to

350   completely replaced by this calcite-REE-rich association (Fig. 5d). These calcite-

351   monazite-(Ce) patches are not restricted to these dykes and occur in less abundance in

352   surrounding calcite carbonatite. The sequence of replacement was apatite replaced by

353   monazite-(Ce) that was later replaced by pink calcite and associated parisite-(Ce) and

354   synchysite-(Ce). Monazite-(Ce) is also rarely replaced by pyrrhotite and magnetite in

355   this carbonatite. The dolomite carbonatite contains patches and crystals of microporous

356   calcite with microinclusions (<2 μm wide) of strontianite ± Ca-REE-Ba-Sr carbonates

357   (possibly burbankite or carbocernaite).

358

359   *Low-Sr dolomite carbonatite*

360

361   The low-Sr dolomite carbonatites are white–grey, massive and dominantly composed of

362   turbid recrystallised, microporous dolomite (≤2 cm long crystals; anhedral with irregular

363   boundaries). Boundaries with the surrounding calcite carbonatite commonly are

364   gradational. Some zones within the carbonatite dykes have a vuggy texture and are weakly

365   mineralised (e.g. 110.5–136.4 m, 303–322.2 m in CDD1; 328.3–396 m in CDD2; Fig. 5e).

366   Vugs (≤~5 cm wide), typically containing ≤1 vol.% REE-bearing minerals, are lined by

367   euhedral coarse dolomite crystals associated with crystals of pyrite–marcasite, quartz,

368   monazite-(Ce), encrustations of very fine-grained platy crystals and crystal groups of the

369   REE-fluorocarbonates parisite-(Ce) and synchysite-(Ce) (+ rare fine acicular groups of a

370   Nb-Ti mineral, probably nioboaeschynite-(Ce)) ± Mg-silicates (talc; Fig. 5f).

371

372   High-REE apatite-monazite-(Ce) rock

373

374   Within the drill hole CDD1, the interval 261.85–275.2 m is composed of weakly–strongly

375   foliated rocks including carbonatite and apatite-monazite-(Ce)-amphibole-talc-rich rocks.

376 Some strongly foliated zones contain ~5–10 vol.% fine–medium grained disseminated

377 zircon (the zircon has yellow SW fluorescence; ~269–269.15 m, 272.5–273 m). This shear

378 zone was intruded by white, massive–fractured dolomite carbonatite dykes and veins, and

379 over the interval 269.2–271.1 m light grey, fine-grained high REE apatite-monazite-(Ce)

380 rocks (containing ≤~25.8 wt% TREO) occur adjacent to these dolomite carbonatite dykes

381 (≤0.142 wt% TREO; Fig. 6). From historical exploration geochemistry, the interval 269–

382 271m is particularly high grade, with 8.29 wt% from 269–270m, and 5.14 wt% TREO from

383 270–271 m (Fig. 3). The apatite-monazite-(Ce) rocks comprise complex intergrowths of

384 apatite and monazite-(Ce) (that varies from thin, elongated crystals to granular in habit) that

385 are overprinted by veins of talc-amphibole-pyrrhotite-dolomite (Fig. 7). Monazite-(Ce) may

386 also occur in a talc–amphibole matrix. The thin, elongated crystals of monazite-(Ce)

387 intergrown with apatite are up to ~0.8 mm long, and the apatite in this association is

388 polycrystalline (variation in extinction angle), turbid and partially altered. In one sample

389 (CDD1-33), this apatite-monazite-(Ce) zone has a sharp contact with an adjacent apatite-

390 rich vein containing patchy to concentrically-zoned, elongated, crystals of apatite (≤3 mm

391 long) aligned approximately perpendicular to the vein margins (Fig. 6).

392   Zones of foliated apatite-talc-monazite-(Ce)-amphibole rock are banded on a cm-scale

393 (e.g. CDD1 265–266 m 3.3 wt% TREO). These include weakly foliated, monazite-(Ce)-

394 talc-rich bands that contain ~40–50 vol.% anhedral–subhedral monazite-(Ce) crystals

395 (≤~1.3 mm long, commonly fractured) in a talc-amphibole-pyrrhotite matrix (Fig. 7b, d).

396 The monazite-(Ce)-talc bands are enclosed by moderately foliated bands of apatite-

397 amphibole-monazite-(Ce)-talc in which the fabric is defined by crystals of green-blue

398 amphibole (richterite, ≤~1.2 mm long) intergrown with fine-grained talc and irregular

399   lenses and grains of pyrrhotite (≤~1.3 mm long). The amphiboles enclose lenses of

400   recrystallised and altered apatite to ~2 mm long, and trains of equant/granular crystals of

401   monazite-(Ce) (≤~0.7 mm long, ≤~5 vol.%). Banding also includes more massive zones of

402   altered and recrystallised apatite that are crosscut by lenses of amphibole (~15 vol.%, ≤~4

403   mm long) and ragged grains and lenses of pyrrhotite ± rare chalcopyrite (≤~0.7 mm long).

404

Geochemistry

406

Apatite chemistry

408

409   Electron microprobe data acquired from two samples of the high-REE apatite-monazite-

410   (Ce) rock (CDD1-29, CDD1-33) and 3 samples of carbonatite are presented in Table 2 and

411   Fig. 8. The high-REE apatite-monazite-(Ce) rock contains areas with zoned apatite crystals

412   (~5 vol.%). Crystal cores, to ~600 μm long, occur in areas of massive uniform apatite in a

413   talc-rich matrix. Apatite cores are REE-rich (Y_2O_3 0.22–0.43 wt%; TREO 4.07–10.1 wt%;

414   SrO 1.22–2.81 wt%) and apatite rims or surrounding apatite in the matrix are Sr-rich (SrO

415   1.78–11.39 wt%) and poor in REEs (TREO ≤2.92 wt%; Y_2O_3 ≤0.12 wt%). Notably, some

416   of these apatite cores exhibit positive Eu anomalies (Eu/Eu*~2.4–8.8; Fig. 8b). Apatite in

417   the carbonatites has distinctive Sr and REE contents, with generally <2 wt% SrO and ≤2.42

418   wt% TREO. Apatite analyses from the high-REE apatite-monazite-(Ce) rock may have low

419   analytical totals which could be due to the effects of hydrothermal alteration or the presence

420   of CO_3^{2-} that has not been determined (Table 2; cf. DeToledo et al. 2004).

421

422   Whole-rock geochemistry

423

424   Whole-rock geochemical data for the CRCC is presented in Tables 3 and 4, and Figs 3 and

425   9 (see also Appendix 1). The high-Sr calcite carbonatite contains from 4800–6060 ppm Sr,

426   from 1.41–3.2 wt% MgO, from 0.18–0.30 wt% MnO, and from 0.42–1.80 wt% P_2O_5. The

427   calcite carbonatites are weakly mineralised, containing 0.138–0.163 wt% TREO (La/Yb_{CN}

428   = 31.6–41.5; La/Nd_{CN} = 1.72–2.23). The pink calcite carbonatite (CDD1-24) has relatively

429   higher Zr and Hf content than other calcite carbonatite samples (Fig. 9b).

430   The high-Sr dolomite carbonatite contains relatively high MnO from 0.683–1.12 wt%,

431   and MgO from 16.1–19 wt% (CDD1-34 contains 12.7 wt% MgO but this sample has a high

432   iron content due to sulfides). Sr content ranges from 4090–6310 ppm, and P_2O_5 from 0.1–

433   0.92 wt%. The TREO content is the lowest of all carbonatites in the complex, ranging from

434   0.071–0.145 wt%, but it exhibits high LREE/HREE ratios (La/Yb_{CN} = 96.5–352; La/Nd_{CN}

435   = 2–3.14). In contrast, the low-Sr dolomite carbonatite (Sr = 38.5–282 ppm) contains lower

436   amounts of Fe and Mn, but higher TREO (MnO = 0.26–0.34 wt%; P_2O_5 = 0.035–0.9 wt%;

437   TREO = 0.124–0.358 wt%). The low-Sr dolomite carbonatite has variable REE content,

438   with La/Yb_{CN} = 38.4–158.4 and La/Nd_{CN} = 1.98–2.73.

439   The high-REE dolomite carbonatite (2) dyke (CDD2-25A) contains 3.43 wt% TREO.

440   It has relatively high P_2O_5 (7.28 wt%) due to its apatite content and very high LREE

441 enrichment (La/Yb$_{CN}$ = 2756; La/Nd$_{CN}$ = 5.8). Unfortunately, insufficient sample was

442 available from the high-REE dolomite carbonatite (1) dyke to undertake whole-rock

443 geochemistry. The high-REE apatite-monazite-(Ce) rock (CDD1-36) is rich in Ca, Sr, and

444 P and is extremely enriched in REEs with ~25.8 wt% TREO, has a high La/Nd$_{CN}$ ratio

445 (~5.4), an extremely high La/Yb$_{CN}$ ratio (30085), and a high abundance of Y (126 ppm).

446 Notably, its chondrite-normalised REE pattern is discordant to the quasi-parallel patterns of

447 the carbonatites sampled (Fig. 9a).

448   Geochemically the primary carbonatites are high in Sr, and relatively low in Ba (≤509

449 ppm) and all carbonatites are low in HFSE (e.g. Zr ≤279 ppm, Nb ≤254 ppm, Hf ≤3.81

450 ppm, Ta ≤7.39 ppm). The Th/U, Nb/Ta and Zr/Hf ratios of the carbonatite samples are

451 quite variable (Table 3) and probably are controlled by zircon and pyrochlore content (Fig.

452 9). In four carbonatite samples Hf content is below detection limits and two carbonatites

453 have anomalously low Zr/Hf ratios with Hf content <0.15 ppm (Table 4). The remaining

454 carbonatite samples have Zr/Hf ratios in the range 25.9–73.2 (average ~43.8), which is

455 similar to the range for the Kovdor and Turiy Mys carbonatites from the Kola Alkaline

456 Province, Russia (36–72; Ivanikov et al. 1998; Verhulst et al. 2000) and exceeds the

457 primitive mantle value (~37). The Zr/Hf ratio of the apatite-amphibole phoscorite (52.5) is

458 similar to the worldwide average of phoscorites and silicocarbonatites (57;

459 Chakhmouradian 2006). The average Zr/Nb ratio of the carbonatites is the same as the

460 worldwide carbonatite average (0.8; Chakhmouradian 2006), and much lower than the

461 Zr/Nb ratio of the phoscorite (~6.39).

462   Y/Ho ratios are close to the primitive mantle value (~27) for the majority of carbonatite

463 samples (21.5–27.1), but the high-Sr calcite carbonatite (CDD2-21A) has Y/Ho = 15.1 and

464   the high-REE dolomite carbonatite dyke (2; CDD2-25A) has a low value of 2.14 and a

465   negative Eu anomaly (Eu/Eu* = 0.62). The high-REE apatite-monazite-(Ce) rock (CCD1-

466   36) also has a relatively low Y/Ho ratio of 17.9.

467   Ga/Ge ratios in a large group of calcite and dolomite carbonatites (n = 6) are on

468   average 5.34 (Table 4), which is slightly above the ratio for the primitive mantle ~3.67.

469   Higher Ga/Ge ratios occur in samples with Al-bearing minerals, and thus a higher Ga

470   content, apart from the late-stage high-REE dolomite carbonatite (CDD2-25A). The tightly

471   constrained nature and consistency of the Ga/Ge ratios for the majority of carbonatite

472   samples suggests that this ratio may reflect the mantle source.

473

474   H-C-O stable isotopes

475

476   Several groupings and trends in the C-O isotope data can be defined for the CRCC samples

477   (Table 5; Fig. 10). High-Sr calcite carbonatites form a group with a range in $\delta^{18}O$ of 7.5 to

478   8.6 ‰ and $\delta^{13}C$ of -4.2 to -4.0 ‰. This group exhibits a positive $\delta^{13}C$ shift (1) at almost

479   constant $\delta^{18}O$ from a theoretical uncontaminated mantle source composition. Seven

480   samples of dominantly dolomite carbonatite (with one sample of calcite carbonatite) define

481   a weak positive trend over the ranges in $\delta^{18}O$ of 8.3 to 12.6 ‰ and $\delta^{13}C$ of -3.4 to -2.2 ‰

482   (shift 2). A group of low-Sr dolomite carbonatite samples (with vuggy textures) have $\delta^{18}O$

483   values from 20.8 to 21.9‰, with a relatively narrow range in $\delta^{13}C$ of -4.3 to -3.6 ‰ (shift 3

484   from the primary carbonatite field). The clinopyroxenite samples define two groups, one

485   with $\delta^{18}O$ values from 11.1 to 11.3 ‰ and $\delta^{13}C$ from -5.6 to -5.4 ‰, and another group

486   with $\delta^{18}O$ from 9.7 to 11.2 ‰ and $\delta^{13}C$ from -4.4 to -3.9 ‰ that includes one amphibole-

487   apatite phoscorite. One further clinopyroxenite sample contains calcite that has experienced

488   a large shift in $\delta^{18}O$ compared to the signature of other clinopyroxenites ($\delta^{18}O = 21.4$ ‰,

489    $\delta^{13}C = -3.8$ ‰). The results of H_2O-contents and stable H isotope analysis of fluid

490   inclusion-hosted H_2O, as well as bulk carbonate C and O isotope compositions for ten

491   carbonate samples from various carbonatites are presented in Table 6 and Fig. 11.

492

493   **Discussion**

494

495   Evolution of the Cummins Range carbonatites

496

497   Current evidence suggests that carbonatite magmas may have evolved from mantle-derived

498   alkali-rich carbonated silicate magmas by some form of fractional crystallization or liquid

499   immiscibility (e.g. Lee and Wylie 1998; Downes et al. 2005; Chakhmouradian and Zaitsev

500   2012). Alternatively, a small number of carbonatites probably were derived directly from

501   the mantle by partial melting of metasomatised peridotite (e.g. Ray et al. 2013;

502   Chakhmouradian and Zaitsev 2012). At Cummins Range, the association of the

503   carbonatites with coeval clinopyroxenite suggests a genetic relationship between the two.

504   No evidence for any form of liquid immiscibilty (e.g. conjugate silicate-carbonate or

505   silicate-phosphate melts, or melt inclusion evidence of two immiscible liquids) involved in

506   the evolution of the Cummins Range carbonatites has been discovered so far, however the

507   operation of fractional crystallization processes is evident from the presence of apatite-

508   phlogopite-magnetite (± ilmenite ± pyrochlore) rich bands within the carbonatites, and

509   cumulate textures in associated phoscorite and clinopyroxenite in parts of the CRCC. The

510   fractionation of REE-poor magnetite, ilmenite, phlogopite and/or diopside, along with

511   dolomite or calcite, is thought to have played a role in the derivation of the late-stage, high-

512   REE dolomite carbonatite dykes at Cummins Range. However, this picture is complicated

513   by the role of apatite in controlling the REE budget in these rocks. Bands of cumulate-

514   textured apatite-amphibole-rich carbonatite are enriched in Zr, Nb, REEs, F, P and Na in

515   comparison to associated calcite carbonatite (compare CDD2-21A and CDD2-27). The

516   increased REE content in the cumulate rock could be related to higher apatite content, but

517   Na-Zr-REE-bearing metasomatic–hydrothermal fluids have also altered these rocks, where

518   zircon and amphiboles appear to overprint the primary fabric and calcite replaces monazite-

519   (Ce) after apatite. One of the cumulate-textured apatite-amphibole phoscorite units (CDD1-

520   22) also is hydrothermally mineralised, with minor fluorite replacing carbonate, and this is

521   reflected in the relatively high Y, HREE and F content of this rock. Therefore, apart from

522   one very low volume parisite-(Ce)-bearing dolomite carbonatite dyke (1), the primary

523   magmatic carbonatites do not appear to have been greatly enriched in REEs by magmatic

524   fractionation processes. Hydrothermal processes probably were of greater importance in

525   enriching the high-REE dolomite carbonatite dyke (2) in LREEs (see below).

526   The HFSE chemistry of the Cummins Range carbonatites shows similarities to

527   carbonatites from the Kola Alkaline Province in Russia (e.g. Zr/Hf and Zr/Nb ratios), but is

528   notably different from post-orogenic carbonatites such as Eden Lake, Canada where the

529   Zr/Nb ratio (24.5; Chakhmouradian et al. 2008) is much higher than the worldwide

530   carbonatite average of 0.8 (Chakhmouradian 2006). In contrast to the low Zr and Hf content

531   of the Cummins Range carbonatites, the associated clinopyroxenite is extremely enriched in

532   these elements (Fig. 3). Therefore, if the primary high-Sr calcite carbonatite was derived

533   from a carbonated silicate parental magma, then the very low Nb, Ta, Zr and Hf content of

534   the carbonatites could be a function of the fractionation of phases such as zirconolite. The

535   relationship between the clinopyroxenite and the carbonatites will be explored in more

536   detail in subsequent work.

537   Stable C and O isotope data for the high-Sr dolomite carbonatites and one high-REE

538   dolomite carbonatite dyke exhibits a significant shift (2; Fig. 10) from the primary

539   carbonatite field that could be indicative of either Rayleigh fractionation, an internal

540   fluid/magma/mineral evolution with the crystallization and cooling of a CO_2-H_2O-bearing

541   magma (see Deines 1989; Demény et al. 2004; Ray and Ramesh 1999, 2000, 2006), the

542   direct assimilation of sedimentary carbonate (e.g. Santos and Clayton 1995), or addition of

543   external carbon by infiltrating fluids (Demény et al. 1998). Rayleigh fractionation appears

544   to be a more likely process in producing shift (2) than the assimilation of sedimentary

545   carbonate given the geological setting of the CRCC, which has intruded the

546   metamorphosed siliciclastic sediments of the Archean Olympio Formation and gneisses of

547   the Paleoproterozoic Lamboo Complex (Andrew 1990). The dolomite carbonatite sample

548   (CR7) that defines the furthest extent of this trend (2) in the CRCC data ($\delta^{18}O$ = 12.6 ‰,

549    $\delta^{13}C$ = -2.2 ‰) is composed of turbid, microporous dolomite and contains minor quartz

550   veining and weak REE mineralization associated with vugs. This suggests that the sample

551   has been hydrothermally altered, and possibly it experienced a positive shift in $\delta^{18}O$ from

552   its primary isotopic composition similar to other hydrothermally altered samples. The high-

553   Sr dolomite carbonatites that fall along this trend (2) have relatively fractionated

554 LREE/HREE patterns (La/Yb$_{CN}$ ~ 96.5–352), along with depletions in the HREEs and Y in

555 comparison to the high-Sr calcite carbonatites and low-Sr dolomite carbonatites (Fig. 9).

556 This includes the dolomite carbonatite dyke (CDD1-37B; $\delta^{18}O$ = 9.1 ‰, $\delta^{13}C$ = -2.9 ‰)

557 associated with the high-REE apatite-monazite-(Ce) rock in CDD1.

558   In the high-REE dolomite carbonatite (CDD2-25), the pink calcite that replaces

559 primary apatite and associated monazite-(Ce) has higher $\delta^{18}O$ than groundmass dolomite.

560 This indicates a shift in $\delta^{18}O$ at relatively constant $\delta^{13}C$ that may have been produced by

561 postmagmatic isotope exchange with a water-rich carbonatitic fluid (cf. Zaitsev et al. 2002)

562 and there is evidence for the exsolution of an aqueous fluid phase indicated by the REE

563 geochemistry of this dyke (low Y/Ho ratio and Eu anomaly; cf. Buhn et al. 2001; Buhn

564 2008). The second high-REE dolomite carbonatite (CDD2-26) has a more extreme $\delta^{18}O$

565 value that suggests hydrothermal alteration similar to shift (3). Both of these dolomite

566 carbonatite dykes exhibit a positive shift in $\delta^{13}C$ (-3 to -3.3 ‰) in comparison to the group

567 of high-Sr calcite carbonatites with $\delta^{13}C$ ~ -4 ‰. This shift may have been produced by

568 Rayleigh fractionation processes as outlined above (shift 2), or by the addition of external

569 carbon in the form of dissolved HCO_3^- or CO_3^{2-} in the infiltrating fluid (Demény et al.

570 1998; Demény et al. 2004).

571   Stable hydrogen isotope compositions of water trapped in inclusions can provide

572 constraints on the origin of fluids as the δD values can significantly differ between primary

573 magmatic water and crustal solutions (Sheppard 1986). The present δD dataset ranges from

574 −54 to −34 ‰ (Fig. 11, Table 6), which is similar to the upper limit of the δD range

575 obtained for the Speewah complex ~330 km NNE of the CRCC (Fig. 1; Czuppon et al.

576 2014). Within this δD range no systematic change was found with the H_2O content (i.e., the

577   amount of inclusion-hosted water; Fig. 11a) of the carbonate samples, thus the degassing

578   and/or mixing processes assumed for the Speewah complex did not affect the Cummins

579   Range rocks. Both the $\delta^{13}C$ and $\delta^{18}O$ data vary independently from the δD values (Fig. 11b,

580   c) suggesting that the evolution of the carbonatite system was not related to mixing of

581   fluids of different origins.

582

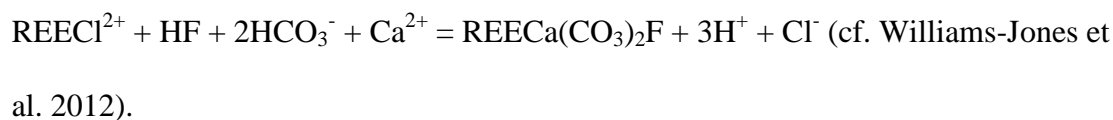583   Hydrothermal processes and REE mineralization

584

585   The highest grade REE mineralization discovered so far beneath the oxidised zone within

586   the CRCC is the unusual apatite-monazite-(Ce) rock intersected in drill hole CDD1 over the

587   interval 261.85–275.2 m (Figs 6, 7). The limited intersection of this REE-rich zone and the

588   broken nature of the drill core does not allow for a comprehensive interpretation of its

589   origin. In the CRCC, those intervals that show the complex intergrowth of fine, elongated

590   monazite-(Ce) crystals in apatite are cut by veins of talc-amphibole that appears to

591   preferentially replace apatite (Fig. 7). Associated foliated rocks in which monazite-(Ce)

592   crystals occur in a talc-amphibole matrix may have developed from more apatite-rich rocks

593   in which the apatite has been replaced by talc during metasomatism/hydrothermal alteration

594   (Fig. 7). Several lines of evidence suggest a hydrothermal origin for the high-REE apatite-

595   monazite-(Ce) rock. Firstly, the texture of the apatite vein adjacent to the apatite-monazite-

596   (Ce) zone illustrated in Fig. 6 indicates hydrothermal growth. In addition, the composition

597   of apatite from the apatite-monazite-(Ce) rock is quite distinct from that of magmatic

598   apatite in associated carbonatites in terms of Sr and REE content (Fig. 8). High-Sr

599   hydrothermal apatite with some textural and compositional similarities to this occurs in

600   hydrothermal phosphate vein-type ores from the southern Central Iberian Zone, Spain

601   (Vindel et al. 2014). De Toledo et al. (2004) also described high-Sr hydrothermal apatites

602   from the Catalao I alkaline-carbonatite complex in Brazil. Positive Eu anomalies in the

603   REE-enriched cores of some zoned apatite crystals in the high-REE apatite-monazite-(Ce)

604   rock suggest crystallization from a Eu-enriched fluid under reducing conditions (cf. Vindel

605   et al. 2014). The very large enrichment in the LREEs evident in the chondrite-normalised

606   REE pattern of the apatite-monazite-(Ce) rock also is consistent with hydrothermal

607   mineralization (Fig. 9a; cf. Ngwenya 1994; Ruberti et al. 2008). The apatite-monazite-(Ce)

608   rock exhibits shifts to higher $\delta^{18}O$ in comparison to an associated dolomite carbonatite dyke

609   (Fig. 10). Texturally, the dolomite in this apatite-monazite-(Ce) rock appears to be

610   associated with talc-amphibole-pyrrhotite veining that crosscuts the apatite-monazite-(Ce)

611   fabric and this shift in $\delta^{18}O$ probably is related to hydrothermal alteration. A factor

612   controlling the occurrence of this high-grade apatite-monazite-(Ce) rock appears to have

613   been the initial presence of an apatite-rich lithology within the shear zone that was subject

614   to subsequent hydrothermal mineralization, where monazite-(Ce) precipitated from REE-

615   rich fluids, and partially replaced and overprinted apatite. The shear zone was the conduit

616   for hydrothermal fluid flow probably contemporaneously with carbonatite emplacement.

617   The timing of this monazite-(Ce) mineralization is presently the subject of further

618   geochronological studies.

619   Hydrothermal alteration at decreasing temperature probably produced the significant

620   shift from the primary carbonatite field seen particularly in the low-Sr, weakly mineralised,

621   dolomite carbonatites (Fig. 10). The widespread hydrothermal dolomitization of

622   carbonatites within the CRCC and the occurrence of associated talc-rich zones within shear

623   zones suggests some similarities to a number of hydrothermal talc deposits, e.g. Ruby

624   Mountains, Montana, USA (Anderson et al. 1990; Brady et al. 1998); Puebla de Lillo,

625   Cantabrian zone, Variscan belt of Iberia, Northern Spain (Tornos and Spiro 2000); and

626   Göpfersgrün, Fichtelgebirge, Germany (Hecht et al. 1999). The talc may have precipitated

627   from Mg and Si-rich hydrothermal fluids at temperatures of approximately 250–400˚C (cf.

628   Hecht et al. 1999). An indication of retrograde hydration is the widespread replacement of

629   diopside by actinolite (uralitization) in the clinopyroxenite. The source of Mg for the

630   formation of talc and dolomite is uncertain but may be the associated clinopyroxenite.

631   It appears that the most important episode of REE mineralization in the Cummins

632   Range carbonatites probably was associated with the late magmatic–hydrothermal phase of

633   carbonatite emplacement, where REEs were mobilised from primary magmatic carbonates

634   (Sr-bearing calcite) and apatite to produce monazite-(Ce) and the REE-fluorocarbonates,

635   parisite-(Ce) and synchysite-(Ce) (cf. Wall and Mariano 1996; Wall and Zaitsev 2004;

636   Chakhmouradian and Zaitsev 2012). A recent review of the transport and deposition of

637   REEs by hydrothermal fluids (Williams-Jones et al. 2012) suggested that a high chloride

638   activity was an important feature of the fluids involved. Chloride species are thought to

639   transport the REEs in most hydrothermal systems (Williams-Jones et al. 2012). At

640   Cummins Range, a possible mechanism for the deposition of the parisite-(Ce) and

641   synchysite-(Ce) could have been:

642     $REECl^{2+} + HF + 2HCO_3^- + Ca^{2+} = REECa(CO_3)_2F + 3H^+ + Cl^-$ (cf. Williams-Jones et

643   al. 2012).

644   The development of vugs in the low-Sr dolomite carbonatite indicates that some

645   dolomite (or calcite) was dissolved probably through reaction with hydrothermal fluids.

646   The following reaction involving the dolomite carbonatite may have increased the HCO_3^-

647   activity and raised the pH of the fluids:

648        $2H^+ + CaMg(CO_3)_2 = Ca^{2+} + Mg^{2+} + 2HCO_3^-,$
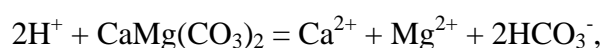
649   resulting in the precipitation of parisite-(Ce) and synchysite-(Ce) in solution cavities (cf.

650   Williams-Jones et al. 2012). Reaction with host carbonatite wall rocks appears to have been

651   a valid mechanism for the precipitation of REE-fluorocarbonates. Monazite-(Ce) most

652   commonly occurs rimming or replacing primary apatite, whereas the REE-fluorocarbonates

653   are generally restricted to a carbonate host. The replacement of apatite by monazite-(Ce) is

654   a common relationship in hydrothermal settings (see Wall and Mariano 1996; Smith et al.

655   1999), and apatite dissolution and monazite-(Ce) precipitation may have proceeded as

656   follows:

657        $Ca_5(PO_4)_3F + 4H^+ + REECl^{2+} = REEPO_4 + 5Ca^{2+} + 2H_2PO_4^- + F^- + Cl^-$

658

659   Relationship between carbonatites and associated clinopyroxenite and phoscorite

660

661   The H-C-O stable isotope data provide some insight into the relationship between the

662   carbonatites and associated clinopyroxenite and phoscorite in the CRCC. Cummins Range

663   exhibits similarities in stable isotope patterns to some of the carbonatite-phoscorite

664   complexes from the Kola Alkaline Province (Demény et al. 2004). Two samples of

665   clinopyroxenite and one of an amphibole-apatite phoscorite have $\delta^{13}C$ values of ~ -4 ‰

666   similar to associated high-Sr calcite carbonatite (Fig. 10). The slight positive shift in $\delta^{18}O$

667   for these samples is consistent with carbonate-silicate isotope exchange at decreasing

668   temperatures (cf. Deines 1989; Demény et al. 2004). One clinopyroxenite sample (CDD2-

669   24) shows a more extreme shift in $\delta^{18}O$ that suggests that it might have been affected by

670   hydrothermal alteration. Of particular interest are the two clinopyroxenite samples (CDD2-

671   11, CDD2-14) that have $\delta^{13}C$ values (-5.62 to -5.38 ‰) more within the range of primary

672   mantle carbonate and similar to values for the Mt Weld carbonatite in Western Australia.

673   The shift in $\delta^{18}O$ for these samples, to place them outside the range for primary igneous

674   carbonate, also could be related to carbonate-silicate isotope exchange at decreasing

675   temperatures (cf. Deines 1989; Demény et al. 2004). These samples do not show the shift in

676   $\delta^{13}C$ that distinguishes the high-Sr calcite carbonatites and some clinopyroxenite and

677   phoscorite samples (shift 1). This could mean that they are derived from a separate mantle

678   source that has been unaffected by source contamination.

679   The relatively high δD values from the Cummins Range carbonatites indicate that the

680   fluid associated with carbonate formation contained a significant amount of crustal

681   component in accordance with the elevated $\delta^{13}C$ values. The normal magmatic $\delta^{18}O$ values

682   (between 6 and 10 ‰) of some of the carbonates at higher-than-mantle C isotopic

683   compositions, however, suggest that the O isotope compositions in these samples were

684   buffered by a magmatic silicate reservoir at high temperature. These observations

685   collectively indicate that the carbonated silicate magma interacted with crustal fluids at

686   depth, and this interaction shifted the H and C isotope compositions due to the relatively

687   high proportion of H and C in the fluid relative to the magma. In contrast to H and C, the O

688   isotope compositions were buffered by the silicate magma from which the carbonate melt

689   and associated fluids were separated.

690

691   Nature and evolution of mantle source regions

692

693   From initial work on a limited range of samples, the Cummins Range carbonatite has

694   quite primitive Sr-Nd isotope compositions suggesting that it is derived from an OIB-type

695   source within the depleted convecting mantle ($^{87}Sr/^{86}Sr = 0.7028–0.7032$; ε Nd = 1.6–2.4;

696   Sun et al. 1986). This source is quite distinct from the radiogenic, enriched mantle sources

697   of the Mesoproterozoic Argyle lamproite (Jaques et al. 1989b) and the Miocene lamproites

698   of the West Kimberley province (McCulloch et al. 1983; Fraser et al. 1985). The high

699   starting $\delta^{13}C$ value of around -4 ‰ for the source of the Cummins Range carbonatites

700   therefore could mean metasomatism of the mantle source region by CO_2 released by a

701   subducted slab (Ray and Ramesh 1999; Zaitsev et al. 2002), or perhaps the removal of a

702   ^{13}C-depleted component within the mantle via isotope fractionation processes (Deines

703   2002).

704   Several authors have proposed that a period of NW-dipping subduction beneath the

705   Kimberley Craton occurred during the Paleoproterozoic, before the eventual collision and

706   amalgamation of the craton with the remainder of the North Australian Craton at

707   approximately 1820 Ma (Myers et al. 1996; Tyler et al. 1999; Griffin et al. 2000). This was

708   the last period during which subduction-related processes would have influenced the mantle

709   beneath the East Kimberley. The ~1800 Ma Hart Dolerite, a widespread series of tholeiitic

710 basaltic and related granophyre intrusions centered in the SE of the Kimberley Craton (Fig.

711 1), is inferred to have been sourced from subduction-modified mantle beneath the

712 Kimberley Craton, and was closely related to plate reorganization in late Paleoproterozoic

713 Australia (Sheppard et al. 2013). Other evidence of plate-margin processes are provided by

714 C isotopic and mineral inclusion studies of eclogitic diamonds from the Argyle lamproite

715 that suggest that they probably formed in subducted oceanic crust that was accreted to the

716 base of the lithosphere in the Proterozoic (Jaques et al. 1989a). Schulze et al. (2013)

717 interpreted an association of light $\delta^{13}C$ in Argyle eclogitic diamonds with high $\delta^{18}O$ values

718 of their garnet and coesite silicate inclusions to indicate a subduction origin. A recent study

719 of the noble gas and C isotopic composition of eclogitic diamonds from Argyle suggests

720 that mixing had occurred between a subducted atmospheric and crustal component and

721 mantle noble gases in their formation (Honda et al. 2012).

722 Further Sr-Nd isotopic analysis is required to examine the observed variation in $\delta^{13}C$ in

723 some clinopyroxenite samples from the CRCC and confirm that they are derived from a

724 separate mantle source unaffected by subduction-related CO_2 metasomatism or the removal

725 of a ^{13}C-depleted component within the mantle.

726 There are several processes that could explain the high δD values of the Cummins

727 Range carbonatites. Degassing of H_2 from the mantle source would leave the residual fluid

728 enriched in deuterium, so the source may acquire a high δD signature (e.g. see Demény et

729 al. 2012). However, this process would not produce high $\delta^{13}C$. Alternatively, interaction

730 with crustal fluids at crustal levels may have taken place, where the emplacement of a

731 carbonated silicate magma may have induced a convective flow in the fluids surrounding

732 the complex. If these fluids had a high-δD signature and the magma interacted with these

733   fluids, the magma, and later the segregated carbonate melt would have a high-δD fluid

734   component too. Mixing of magmatic fluids and waters circulating in the surrounding

735   country rocks may well have produced a fluid with δD around -40 ‰ as observed. This is

736   possible, as we see appropriate fluid compositions regionally, for example at Speewah

737   (Czuppon et al. 2014), but in this case the C and O isotope compositions should show at

738   least a slight change with δD. No such correlation is evident in Fig. 11. The preservation of

739   primitive Sr and Nd isotope compositions in the Cummins Range carbonatite would also

740   argue against significant exchange with crustal fluids in this way. Finally, the subduction

741   and devolatilization of oceanic crust may have provided D-enriched fluids that could, for

742   example, have metasomatised the mantle wedge (e.g. Giggenbach 1992). The release of

743   CO_2 and H_2O from a subducting slab would produce high δD and $\delta^{13}C$ in the

744   metasomatised mantle, but the O isotope composition would be buffered by the silicate

745   mass. CO_2-H_2O fluids without melt may not contain significant amounts of Sr and Nd, so

746   the magma's Sr-Nd isotope compositions would remain intact. Therefore it appears that the

747   δD signature of the Cummins Range carbonatites could be a further indication subduction-

748   related metasomatism of the mantle source.

749

Summary

751

752   The CRCC was emplaced at the junction of the Paleoproterozoic Halls Creek and King

753   Leopold paleo-orogenic belts at the margin of the Kimberley Craton probably during a

754   phase of Neoproterozoic extension. Trace-element geochemistry suggests that the

755   carbonatites have affinities to rift-related carbonatites (cf. Chakhmouradian 2009) and

756   generally are not greatly enriched in the REEs (Fig. 9a). The Cummins Range carbonatites

757   follow an intrusive sequence where early calcite carbonatite, possibly derived from a

758   carbonated silicate parental magma by fractional crystallization, has been intruded by late-

759   stage dolomite carbonatites with higher REE content (Fig. 12; cf. Wall and Mariano 1996).

760   The shift in C-O stable isotope data from the primary carbonatite field for the high-Sr

761   dolomite carbonatites and a high-REE dolomite carbonatite is consistent with a process of

762   Rayleigh fractionation with magma crystallization and cooling. These dolomite carbonatites

763   may have been derived from the calcite carbonatites through the fractionation of phases

764   such as dolomite and apatite. Hydrothermal and metasomatic processes, probably involving

765   fluids exsolved from the carbonatites, produced widespread dolomitization of the

766   carbonatites and high-grade REE mineralization in a late-stage dolomite carbonatite dyke

767   and in shear zone-hosted apatite-monazite-(Ce) rocks. The relatively high δD values (–54 to

768   –34 ‰) of H_2O derived from carbonatites from the CRCC indicate that the fluids associated

769   with carbonate formation contained a significant amount of crustal component in

770   accordance with the elevated $\delta^{13}C$ values (~ -4 ‰). The high δD and $\delta^{13}C$ signature of the

771   carbonatites may have been produced by CO_2-H_2O metasomatism of the mantle source

772   during Paleoproterozoic subduction beneath the eastern margin of the Kimberley Craton.

773

Acknowledgements

774   **Acknowledgements**

775

788

References

790

791 Anderson DL, Mogk DW, Childs JF (1990) Petrogenesis and timing of talc formation in

792   the Ruby Range, southwestern Montana. Economic Geology 85:585–600.

793 Andrew R (1990) Cummins Range Carbonatite. In: Hughes FE (ed) Geology of the Mineral

794   Deposits of Australia and Papua New Guinea. AusIMM, Melbourne, pp 711-713

795 Belousova EA, Griffin WL, O'Reilly SY, Fisher N (2002) Igneous zircon: trace element

796   composition as an indicator of source rock type. Contrib Mineral Petrol 143:602–622.

797   doi: 10.1007/s00410-002-0364-7

798 Brady JB, Cheney JT, Rhodes AL, Vasquez A, Green C, Duvall M, Kogut A, Kaufman L,

799   Kovaric D (1998) Isotope geochemistry of Proterozoic talc occurrences in Archean

800   marbles of the Ruby Mountains, southwest Montana, USA. Geol Mat Res 1:1–41.

801 Bühn B, Wall F, Le Bas MJ (2001) Rare-earth element systematics of carbonatitic

802   fluorapatites, and their significance for carbonatite magma evolution. Contrib Mineral

803   Petrol 141(5):572–591

804 Bühn B (2008) The role of the volatile phase for REE and Y fractionation in low-silica

805   carbonate magmas: implications from natural carbonatites, Namibia. Mineral Petrol

806   92(3-4):453–470

807 Cawood PA, Korsch RJ (2008) Assembling Australia: Proterozoic building of a continent.

808   Precamb Res 166:1–38

809 Chakhmouradian AR (2009) The geochemistry of carbonatites revisited: Two major types

810   of continental carbonatites and their trace-element signatures. EGU General

811   Assembly 2009, held 19-24 April, 2009 in Vienna, Austria http://meetings copernicus

812   org/egu2009, p 10806 11:10806

813 Chakhmouradian AR, Böhm CO, Demény A, Reguir EP, Hegner E, Creaser RA, Halden

814   NM, Yang P (2009) "Kimberlite" from Wekusko Lake, Manitoba: Actually a

815   diamond-indicator-bearing dolomite carbonatite. Lithos 112:347–357. doi:

816   10.1016/j.lithos.2009.03.039

817 Chakhmouradian AR, Mumin A, Demény A, Elliott B (2008) Postorogenic carbonatites at

818   Eden Lake, Trans-Hudson Orogen (northern Manitoba, Canada): geological setting,

819   mineralogy and geochemistry. Lithos 103:503–526

820 Chakhmouradian AR, Zaitsev AN (2012) Rare Earth Mineralization in Igneous Rocks:

821   Sources and Processes. Elements 8(5):347–353

822   Czuppon Gy, Ramsay RR, Özgenc I, Demény A, Gwalani LG, Rogers K, Eves A, Papp L,

823   Palcsu L, Berkesi M, Downes PJ (2014) Stable (H, O, C) and noble-gas (He and Ar)

824   isotopic compositions from calcite and fluorite in the Speewah Dome, Kimberley

825   Region, Western Australia: Implications for the conditions of crystallization and

826   evidence for the influence of crustal-fluid mixing. Mineral Petrol doi:

827   10.1007/s00710-014-0333-7.

828   Demény A (1995) H isotope fractionation due to hydrogen-zinc reactions and its

829   implications on D/H analysis of water samples. Chem Geol 121:19–25

830   Demény A, Ahijado A, Casillas R, Vennemann TW (1998) Crustal contamination and

831   fluid/rock interaction in the carbonatites of Fuerteventura (Canary Islands, Spain): a

832   C, O, H isotope study. Lithos 44(3-4):101–115

833   Demény A, Sitnikova MA, Karchevsky PI (2004) Stable C and O isotope compositions of

834   carbonatite complexes of the Kola alkaline province: phoscorite-carbonatite

835   relationships and source compositions. In: Wall F, Zaitsev AN (eds) Phoscorites and

836   Carbonatites from Mantle to Mine. Mineralogical Society Series 10, Mineralogical

837   Society, London, pp 407–431

838   Demény A, Siklósy Z (2008) Combination of off-line preparation and continuous flow

839   mass spectrometry: D/H analyses of inclusion waters. Rapid Comm Mass Spect

840   22:1329-1334

841   Demény A, Harangi S, Vennemann TW, Casillas R, Horváth P, Milton AJ, Mason PRD,

842   Ulianov A (2012) Amphiboles as indicators of mantle source contamination:

843   Combined evaluation of stable H and O isotope compositions and trace element

844   ratios. Lithos 152:141–156. doi:10.1016/j.lithos.2012.07.001

845   De Toledo M, Lenharo S, Ferrari V, Fontan F, De Parseval P, Leroy G (2004) The

846   compositional evolution of apatite in the weathering profile of the Catalão I alkaline-

847   carbonatitic complex, Goiás, Brazil. Can Mineral 42:1139–1158.

848   Downes H, Balaganskaya E, Beard AD, Liferovich RP, Demaiffe D (2005) Petrogenetic

849   processes in the ultramafic, alkaline and carbonatitic magmatism in the Kola Alkaline

850   Province: A review. Lithos 85:48–75. doi: 10.1016/j.lithos.2005.03.020

851   Eggins SM, Woodhead JD, Kinsley LPJ, Mortimer GE, Sylvester P, McCulloch MT, Hergt

852   JM, Handler MR (1997) A simple method for the precise determination of ≥ 40 trace

853   elements in geological samples by ICPMS using enriched isotope internal

854   standardisation. Chem Geol 134:311–326. doi: http://dx.doi.org/10.1016/S0009-

855   2541(96)00100-3

856   Fraser KJ, Hawkesworth CJ, Erlank AJ, Mitchell RH, Scott-Smith BH (1985) Sr, Nd and

857   Pb isotope and minor element geochemistry of lamproites and kimberlites. Earth

858   Planet Sci Lett 76:57–70.

859   Geological Survey of Western Australia (2011) Investment opportunities–Rare Earths.

860   http://www.hastingsraremetals.com/wp-content/uploads/2012/07/2011-10-03-7_wa-

861   mines-dept-rare-earth-october-2011.pdf. Accessed 20 December 2013

862   Giggenbach WF (1992) Isotopic shifts in waters from geothermal and volcanic systems

863   along convergent plate boundaries and their origin. Earth Planet Sci Lett 113:495–

864   510

865 Graham S, Lambert D, Shee S (2004) The petrogenesis of carbonatite, melnoite and

866   kimberlite from the Eastern Goldfields Province, Yilgarn Craton. Lithos 76:519–533

867 Griffin TJ, Page RW, Sheppard S, Tyler IM (2000) Tectonic implications of

868   Palaeoproterozoic post-collisional, high-K felsic igneous rocks from the Kimberley

869   region of northwestern Australia. Precamb Res 101:1–23

870 Hassan LY (2000) Mineral occurrences and exploration potential of the East Kimberley.

871   Geological Survey of Western Australia Report 74, Department of Minerals and

872   Energy, Perth, 60 pp

873 Hecht L, Freiberger R, Gilg HA, Grundmann G, Kostitsyn YA (1999) Rare earth element

874   and isotope (C, O, Sr) characteristics of hydrothermal carbonates: genetic

875   implications for dolomite-hosted talc mineralization at Göpfersgrün (Fichtelgebirge,

876   Germany). Chem Geol 155:115–130.

877 Honda M, Phillips D, Kendrick MA, Gagan MK, Taylor WR (2012) Noble gas and carbon

878   isotope ratios in Argyle diamonds, Western Australia: Evidence for a deeply

879   subducted volatile component. Australian J Earth Sci 59(8):1135-1142

880 Jaques AL, Lewis JD, Smith CB (1986) The kimberlites and lamproites of Western

881   Australia. Geological Survey of Western Australia Bulletin 132, 268 pp

882 Jaques AL, Hall AE, Sheraton JV, Smith CB, Sun SS, Drew R, Foudoulis C, Ellingsen K

883   (1989a) Composition of crystalline inclusions and C-isotopic composition of Argyle

884   and Ellendale diamonds. In: Ross J et al. (eds) Kimberlites and Related Rocks: Their

885   Crust/Mantle Setting, Diamonds and Diamond Exploration. Geol Soc Australia Spec

886   Publ 14, vol. 2, pp 966–989

887   Jaques AL, Sun SS, Chappell BW (1989b) Geochemistry of the Argyle (AK1) lamproite

888   pipe, Western Australia. In: Ross J et al. (eds) Kimberlites and Related Rocks: Their

889   Composition, Occurrence, Origin and Emplacement. Geol Soc Australia Spec Publ

890   14, vol. 1, pp 170–188

891   Jaques AL, Milligan (2004) Patterns and controls on the distribution of diamondiferous

892   intrusions in Australia. Lithos 77(1-4):783-802

893   Jenner FE, O'Neill HS-C (2012) Major and trace analysis of basaltic glasses by laser-

894   ablation ICP-MS. Geochem. Geophys. Geosyst. 13, Q03003,

895   doi:10.1029/2011GC003890.

896   Johnson SP (2013) The birth of supercontinents and the Proterozoic assembly of Western

897   Australia. Geological Survey of Western Australia, Perth, 78pp

898   Keller J, Hoefs J (1995) Stable isotope characteristics of recent natrocarbonatites from

899   Oldoinyo Lengai. In: Bell K, Keller J (eds) Carbonatite volcanism: Oldoinyo Lengai

900   and the petrogenesis of natrocarbonatites. Springer Verlag, Berlin, pp 113–123

901   Kimberley Rare Earths (2012) Annual report to shareholders. Perth, Western Australia, pp

902   1–54. http://anovametals.com.au/wp-

903   content/uploads/2012/11/206_KRE_2012_Annual_Report_to_Shareholders_Final.pd

904   f. Accessed 20 December 2013

905   Krasnova NI, Petrov TG, Balaganskaya EG, Garcia D, Moutte J, Zaitsev AN, Wall F

906   (2004) Introduction to phoscorites: occurrence, composition, nomenclature and

907   petrogenesis. In: Wall F and Zaitsev AN (eds), Phoscorites and Carbonatites from

908   Mantle to Mine: the key example of the Kola Alkaline Province. Mineralogical

909   Society Series 10, Mineralogical Society, London, pp 45–74

910   Lee W, Wyllie PJ (1998) Processes of crustal carbonatite formation by liquid immiscibiluty

911   and differentiation, elucidated by model systems. J Petrol 39:2005–2013

912   Luguet A, Jaques AL, Pearson DG, Smith CB, Bulanova GP, Roffey SL, Rayner MJ,

913   Lorand JP (2009) An integrated petrological, geochemical and Re–Os isotope study

914   of peridotite xenoliths from the Argyle lamproite, Western Australia and implications

915   for cratonic diamond occurrences. Lithos 112:1096-1108

916   McCulloch MT, Jaques AL, Nelson D, Lewis JD (1983) Nd and Sr isotopes in kimberlites

917   and lamproites from Western Australia: an enriched mantle origin. Nature 302: 400–

918   403

919   Myers JS, Shaw RD, Tyler IM (1996) Tectonic evolution of Proterozoic Australia.

920   Tectonics 15:1431–1446

921   Nelson DR, Chivas AR, Chappell BW, McCulloch MT (1988) Geochemical and isotopic

922   systematics in carbonatites and implications for the evolution of ocean-island sources.

923   Geochim Cosmochim Acta 52(1):1–18

924   Ngwenya BT (1994) Hydrothermal rare earth mineralisation in carbonatites of the Tundulu

925   complex, Malawi: Processes at the fluid/rock interface. Geochimica Cosmochim Acta

926   58(9):2061–2072

927 Norrish K, Chappell BW (1977) X-ray fluorescence spectrometry. In: Zussman J (ed)

928 Physical methods in determinative mineralogy, 2nd edn. Academic Press, London, pp

929 201–272.

930 Norrish K, Hutton JT (1969) An accurate X-ray spectrographic method for the analysis of a

931 wide range of geological samples. Geochim Cosmochim Acta 33(4):431–453

932 Palme H, O'Neill HStC (2005) Cosmochemical estimates of mantle composition. In: RW

933 Carlson (ed) The Mantle and Core, Vol. 2 Treatise on Geochemistry. Elsevier–

934 Pergamon, Oxford, pp 1–38

935 Paton, C, Hellstrom, J, Bence, P, Woodhead, J, Hergt, J (2011) Iolite: Freeware for the

936 visualisation and processing of mass spectrometric data. J. Anal. At. Spectrom.

937 26:2508-2518

938 Pidgeon RT, Smith CB, Fanning CM (1986) The ages of kimberlite and lamproite

939 emplacement in Western Australia. In: 4th International Kimberlite Conference,

940 Perth, 1986, Geol. Soc. Aust. Abstr. 16, pp 136-138

941 Pyke J (2000) Minerals laboratory staff develops new ICP-MS preparation method. Aust.

942 Geol. Survey Org. Res. Newslett. 33:12–14

943 Ray J, Ramesh R (1999) Evolution of carbonatite complexes of the Deccan flood basalt

944 province: stable carbon and oxygen isotopic constraints. J Geophys Res 104:29471–

945 29483

946 Ray J, Ramesh R (2000) Rayleigh fractionation of stable isotopes from a multicomponent

947 source. Geochim Cosmochim Acta 64:299–306

948 Ray JS, Ramesh R (2006) Stable Carbon and Oxygen Isotopic Compositions of Indian

949   Carbonatites. Internat Geol Rev 48:17–45. doi: 10.2747/0020-6814.48.1.17

950 Ray JS, Pande K, Bhutani R, Shukla AD, Rai VK, Kumar A, Awasthi N, Smitha RS, Panda

951   DK (2013) Age and geochemistry of the Newania dolomite carbonatites, India:

952   implications for the source of primary carbonatite magma. Contrib Mineral Petrol

953   166:1613–1632. doi: 10.1007/s00410-013-0945-7

954 Richards MN (1984) Annual report for 1983 on exploration licence 80/113, Cummins

955   Range, Mt. Bannerman, SE52-13, Western Australia. CRA Exploration Pty. Ltd.

956   Report to West Australian Department of Mines and Petroleum, A14632, CRAE Ref.

957   No. 12981, 40 pp

958 Richards MN (1985) Annual report for 1984 on exploration licence 80/113, Cummins

959   Range, Mt. Bannerman, SE52-13, Western Australia, Volume 1. CRA Exploration

960   Pty. Ltd. Report to West Australian Department of Mines and Petroleum, A16631,

961   CRAE Ref. No. 13612, 20 pp

962 Ruberti E, Enrich GER, Gomes CB, Comin-Chiaramonti P (2008) Hydrothermal REE

963   fluorocarbonate mineralization at Barra do Itapirapua, a multiple stockwork

964   carbonatite, southern Brazil. Can Mineral 46(4):901–914

965 Sanders TS (1999) Mineralization of the Halls Creek Orogen, east Kimberley region,

966   Western Australia. Geological Survey of Western Australia Report 66, Department of

967   Minerals and Energy, Perth, 44 pp

968 Santos R, Clayton RN (1995) Variations of oxygen and carbon isotopes in carbonatites: a

969   study of Brazilian alkaline complexes. Geochim Cosmochim Acta 59:1339–1352.

970   Schulze D, Harte B, Page FZ, Valley JW, Channer DMDeR, Jaques AL (2013)

971   Anticorrelation between low $\delta^{13}C$ of eclogitic diamonds and high $\delta^{18}O$ of their coesite

972   and garnet inclusions requires a subduction origin. Geology 41:455–458

973   Shapiro LM, Brannock WW (1962) Rapid analysis of silicate, carbonate and phosphate

974   rocks. US Geological Survey Bulletin 1144-A. US Government Printing Office.

975   Sheppard S (1986) Characterization and isotopic variations in natural waters. In: Valley

976   JW, Taylor Jr HP, O'Neil JR (eds) Reviews in Mineralogy 16, Stable isotopes in high

977   temperature geological processes. Mineral Soc Amer, pp 165-184

978   Sheppard S, Page RW, Griffin TJ, Rasmussen B, Fletcher IR, Tyler IM, Kirkland CL,

979   Wingate MTD, Hollis JA, Thorne AM (2012) Geochronological and isotopic

980   constraints on the tectonic setting of the c. 1800 Ma Hart Dolerite and the Kimberley

981   and Speewah Basins, Northern Western Australia. Geological Survey of Western

982   Australia Record 2012/7, 28pp

983   Spötl C, Vennemann TW (2003) Continuous-flow IRMS analysis of carbonate minerals.

984   Rapid Commun Mass Spectrom 17:1004-1006

985   Sun S-S, Jaques AL, McCulloch MT (1986) Isotopic evolution of the Kimberley Block,

986   Western Australia. In: 4th International Kimberlite Conference, Perth, 1986, Geol.

987   Soc. Aust. Abstr. 16, pp 346-348

988   Taylor Jr HP, Frechen J, Degens ET (1967) Oxygen and carbon isotope studies of

989   carbonatites from the Laacher See District, West Germany and the Alno District,

990   Sweden. Geochim Cosmochim Acta 31:407–430

991   Tornos F, Spiro BF (2000) The geology and isotope geochemistry of the talc deposits of

992   Puebla de Lillo (Cantabrian Zone, Northern Spain). Economic Geology 95:1277–

993   1296.

994   Tyler IM, Page RW, Griffin TJ (1999) Depositional age and provenance of the Marboo

995   Formation from SHRIMP U–Pb zircon geochronology: implications for the early

996   Palaeoproterozoic tectonic evolution of the Kimberley region, Western Australia.

997   Precamb Res 95:225–243

998   Wall F, Mariano AN (1996) Rare earth minerals in carbonatites: a discussion centered on

999   the Kangankunde carbonatite, Malawi. In: Jones AP, Wall F, Williams CT (eds) Rare

1000   Earth Minerals: Chemistry, Origin and Ore Deposits. Mineralogical Society Series 7,

1001   Mineralogical Society, London, pp 193-225

1002   Wall F, Zaitsev AN (2004) Rare earth minerals in Kola carbonatites. In: Wall F, Zaitsev

1003   AN (eds) Phoscorites and Carbonatites from Mantle to Mine: The Key Example of

1004   the Kola Alkaline Province. Mineralogical Society Series 10, Mineralogical Society,

1005   London, pp 341-373

1006   Williams-Jones AE, Migdisov AA, Samson IM (2012) Hydrothermal Mobilisation of the

1007   Rare Earth Elements - a Tale of "Ceria" and "Yttria". Elements 8(5): 355-360

1008   Zaitsev AN, Demény A, Sindern S, Wall F (2002) Burbankite group minerals and their

1009   alteration in rare earth carbonatites--source of elements and fluids (evidence from CO

1010   and Sr-Nd isotopic data). Lithos 62:15–33

1011

1012   **Appendix 1: Supplementary data**

1013

1014   Exploration whole-rock geochemistry

1015

1016   The graphic drill logs of drill holes CDD1 (Fig. 3) and CDD2 (red circles indicate the

1017   positions of late-stage, high-REE dolomite carbonatite dykes) were constructed using

1018   historical exploration whole-rock geochemical analyses undertaken in 1984 by Pilbara

1019   Laboratories in Perth, on behalf of CRA Exploration (Richards, 1985). These partial

1020   analyses were carried out by inductively-coupled plasma emission spectroscopy (ICP). Full

1021   details of the analytical procedures are described by Richards (1985). This report is

1022   available for download from the Western Australian Department of Mines and Petroleum

1023   website (http://www.dmp.wa.gov.au/launch/wamex/). The full dataset for drill holes CDD1

1024   and CDD2 is presented here. A plan illustrating a possible structural control on the

1025   orientation of the oxidised zone REE orebody in the CRCC is included (courtesy of

1026   Kimberley Rare Earths).

1027

1028   **Figure Captions**

1029   **Fig. 1** Geological map showing the location of the Cummins Range Carbonatite Complex,

1030   Kimberley region, Western Australia (1:2500000 Geological Survey of Western Australia

1031   2014, extracted from GeoVIEW.WA on 05/06/2014. Perth, Western Australia: Department

1032   of Mines and Petroleum.)

1033

1034   **Fig. 2** Geological map of the Cummins Range Carbonatite Complex (1:5000). Drill holes

1035   CDD001, NRC035, NRC058: azimuth 180˚ (mag.), inclination 60˚. CDD002: azimuth 270˚

1036   (mag.), inclination 60˚. Geology modified after Richards (1985) and Andrew (1990) and

1037   based on company drilling. Only the locations of drill holes sampled for use in this study

1038   are shown.

1039

1040   **Fig. 3** Graphic log of drill hole CDD1. Red circles indicate the position of high-REE

1041   apatite-monazite-(Ce) rock associated with dolomite carbonatite dykes within a shear zone.

1042

1043   **Fig. 4 a** Pink high-Sr calcite (cc) carbonatite containing a zircon megacryst (zrc) in an

1044   apatite (ap)-amphibole-phlogopite-pyrochlore lamina, associated with magnetite (mt) and

1045   dolomite (dol) (CDD1 323.9 m). **b** Calcite carbonatite containing large crystals of

1046   magnetite, as well as amphibole (amp) and apatite (CDD2-4, 88.7 m). **c** High-Sr calcite

1047   carbonatite containing apatite, phlogopite (phl) and magnetite overprinted by metasomatic

1048   amphibole crystals (CDD2-21, 399.95 m). **d** Strongly foliated dolomite carbonatite

1049   containing a composite zircon-dolomite porphyroblast (py – pyrite; CR5, CDD1 204.35 m).

1050

1051 **Fig. 5 a** Grey, late stage, high-REE dolomite carbonatite (par – parisite-(Ce), dol –

1052 dolomite, py – pyrite; CDD2-26, 225.2 m). **b** Intergrown crystals of parisite-(Ce) and

1053 aeschynite-(Ce) (aesc) in dolomite carbonatite (note parisite-(Ce) overgrowths on primary

1054 crystal of parisite-(Ce); CDD2-26). **c** Grey, late stage, high-REE dolomite carbonatite dyke

1055 intruding white high-Sr calcite carbonatite (CDD2-25, 397.35 m). Contains patches of pink

1056 calcite-monazite-(Ce) (cc-mz) replacing apatite (ap, phl – phlogopite, amp – amphibole). **d**

1057 Calcite and monazite-(Ce) (mz) replacing apatite in high-REE dolomite carbonatite

1058 (CDD2-25; SEM-BSE image). **e** White low-Sr dolomite carbonatite containing vugs

1059 (CDD2-8, 152 m). **f** Crystals of synchysite-(Ce) (syn) and dolomite lining vug in low-Sr

1060 dolomite carbonatite (CDD2-18, 328.78 m).

1061

1062 **Fig. 6** Boundary between high REE apatite-monazite-(Ce) rock (ap-mz) and an adjacent

1063 comb-textured apatite vein with a dolomite (dol) carbonatite vein at the bottom of the

1064 image (thin section in transmitted light; CDD1, 270.33 m).

1065

1066 **Fig. 7 a** Texture of complex intergrowths in apatite-monazite-(Ce) rock (CDD1-33, 270.33

1067 m; ap – apatite, mz – monazite-(Ce)). **b** Crystals of monazite-(Ce) in talc-amphibole (amp)

1068 matrix (CDD1-29, 265.3 m). **c** BSE image showing texture of complex monazite-(Ce)-

1069 apatite intergrowths (CDD1-33; pyrr – pyrrhotite). **d** BSE image showing texture of

1070 foliated monazite-(Ce)-amphibole-talc rock (CDD1-29). **e** Element map of complex

1071 monazite-(Ce)-apatite intergrowths illustrated in **c**. Red – apatite (P); purple – monazite-

1072   (Ce) (Ce); green – talc, amphibole (Si); light blue – pyrrhotite (S); black – dolomite. **f** BSE

1073   image illustrating further complex intergrowths of monazite-(Ce) and apatite (CDD1-33).

1074

1075   **Fig. 8 a** SrO versus TREO, and **b** Chondrite-normalised REE patterns, for apatite from the

1076   high-REE apatite-monazite-(Ce) rock and carbonatites from the CRCC.

1077

1078   **Fig. 9 a** Chondrite-normalised REE patterns for the Cummins Range carbonatites. Average

1079   magnesiocarbonatite from Chakhmouradian et al. (2009). **b** Primitive mantle-normalised

1080   trace element diagram for the Cummins Range carbonatites (normalising data from Palme

1081   and O'Neill (2005)).

1082

1083   **Fig. 10** Stable carbon and oxygen isotope compositions (in ‰ relative to V-PDB and V-

1084   SMOW, respectively) for the Cummins Range carbonatite complex. Data for the Mt Weld

1085   carbonatite are from Nelson et al. (1988) and Graham et al. (2004). Boxes indicate the

1086   'primary carbonatite fields' of Taylor et al. (1967; black) and Keller and Hoefs (1995;

1087   grey).

1088

1089   **Fig. 11** H_2O-contents (in ppm) and stable hydrogen isotope compositions of fluid inclusion-

1090   hosted H_2O (in ‰ relative to V-SMOW), as well as bulk carbonate C and O isotope

1091   compositions (in ‰ relative to V-PDB and V-SMOW, respectively) for ten carbonate

1092   samples from the Cummins Range carbonatites. **a** δ D versus H_2O contents trapped in fluid

1093   inclusions in host carbonates. **b** and **c**: δ D values of inclusion-hosted water versus δ ^{13}C

1094   (**b**) and δ ^{18}O (**c**) values of the host carbonates.

1095

1096   **Fig. 12** Schematic diagram illustrating the evolution of the CRCC.

Figure 1
Click here to download high resolution image

Figure 1

Figure 2
Click here to download high resolution image

Geology

Iron Oxide Collapse Breccia
(Iron oxide - clay rich siliceous rock after carbonatite)

Carbonatite & Phlogopite - Amphibole Clinopyroxenite (Carbonatite with variably metasomatised clinopyroxenite containing extensive phlogopite, amphibole and carbonate)

Clinopyroxenite

Chlorite Schist
(Country rock enclave)

Gneiss - Lamboo Complex

○ **Drill Hole (other)**

● **Diamond Drill Hole**

N

Figure 3
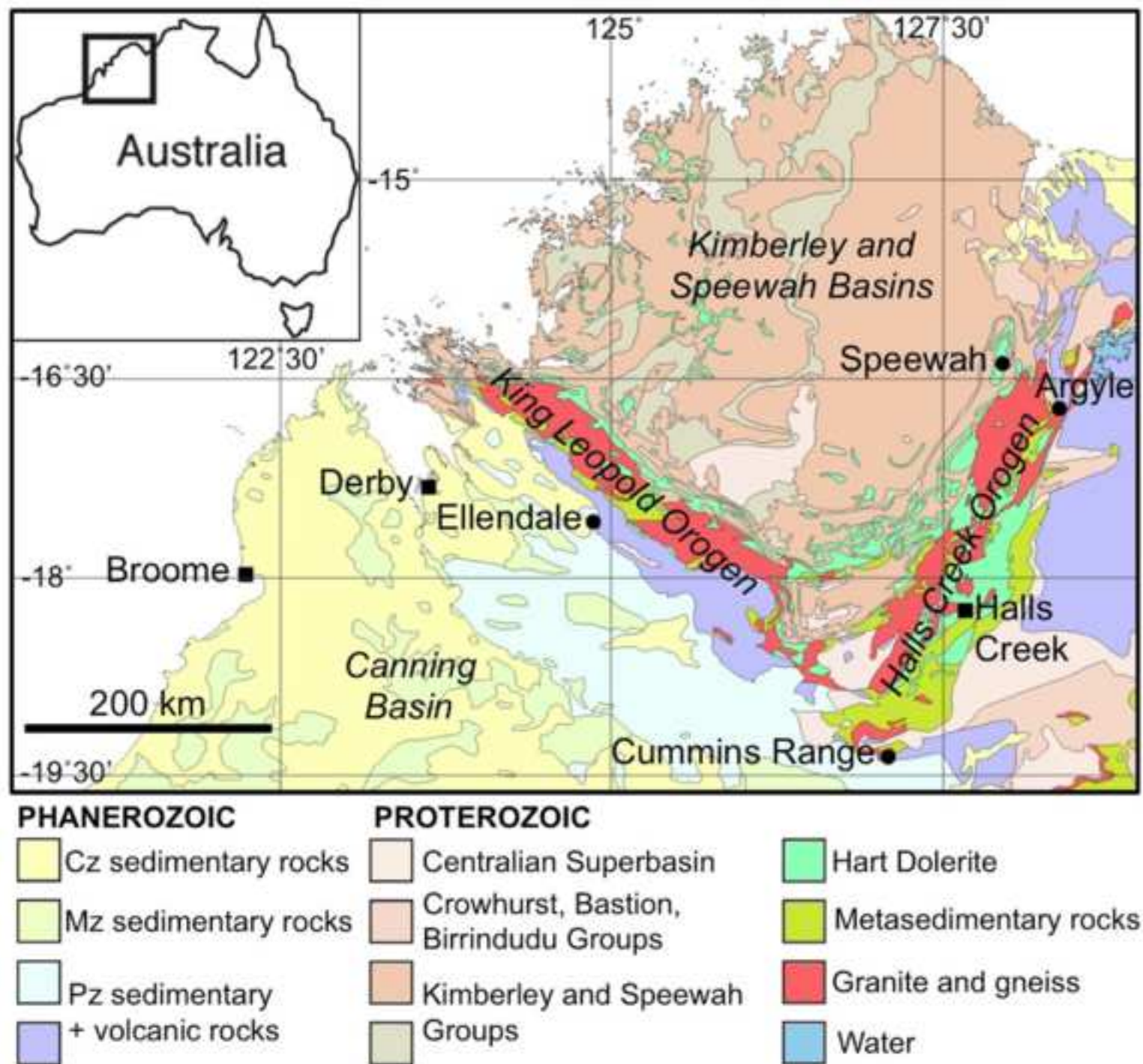Click here to download high resolution image
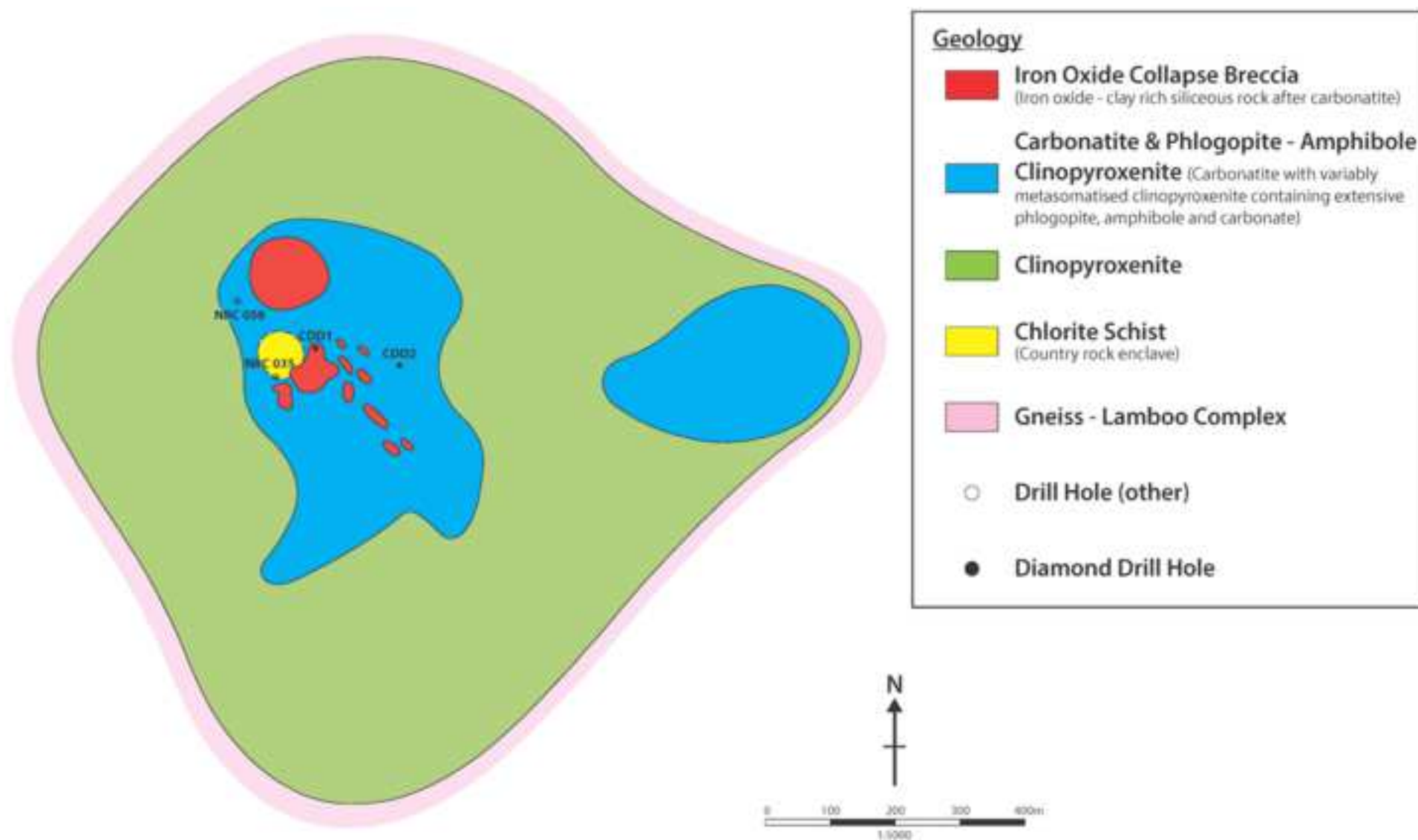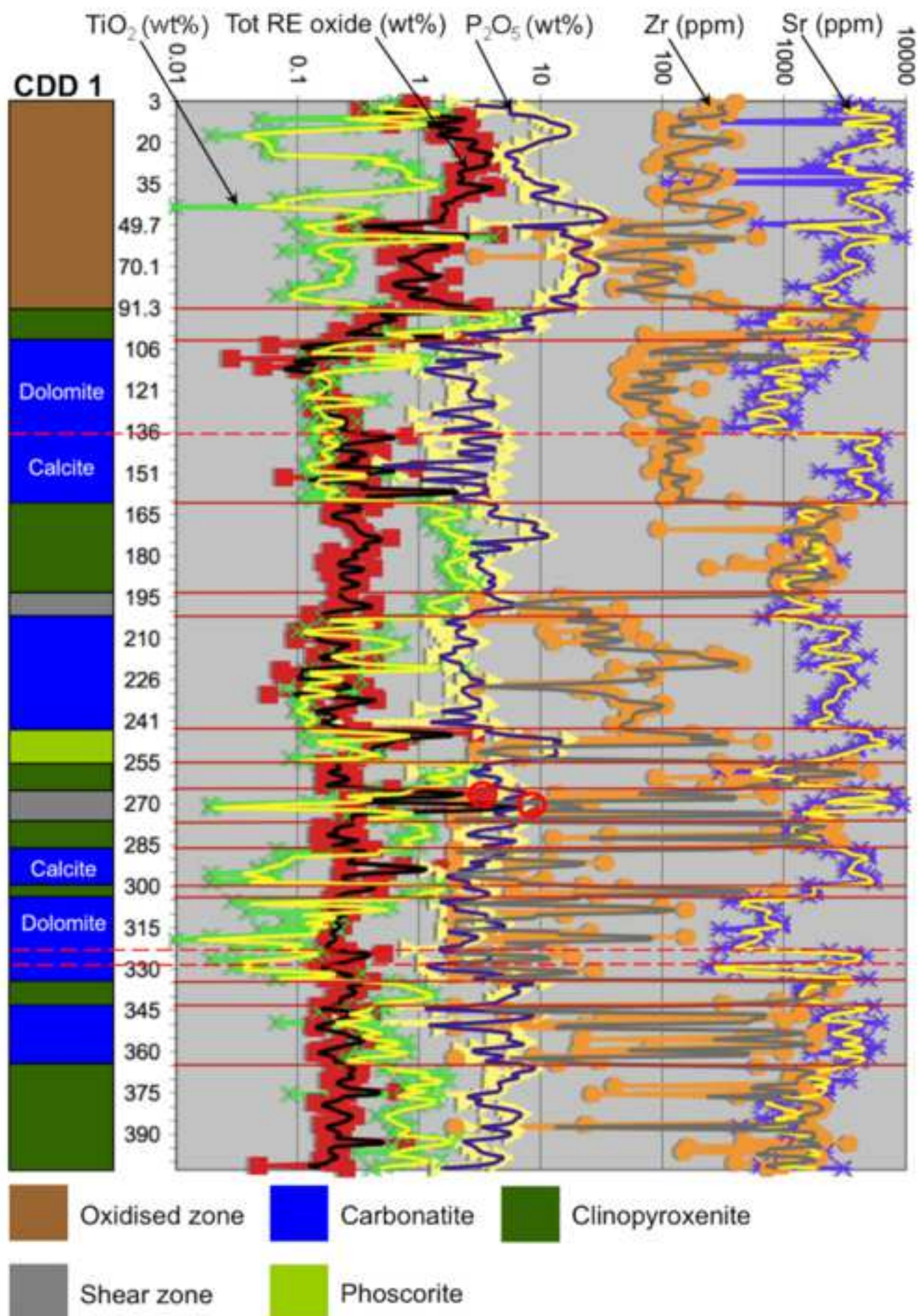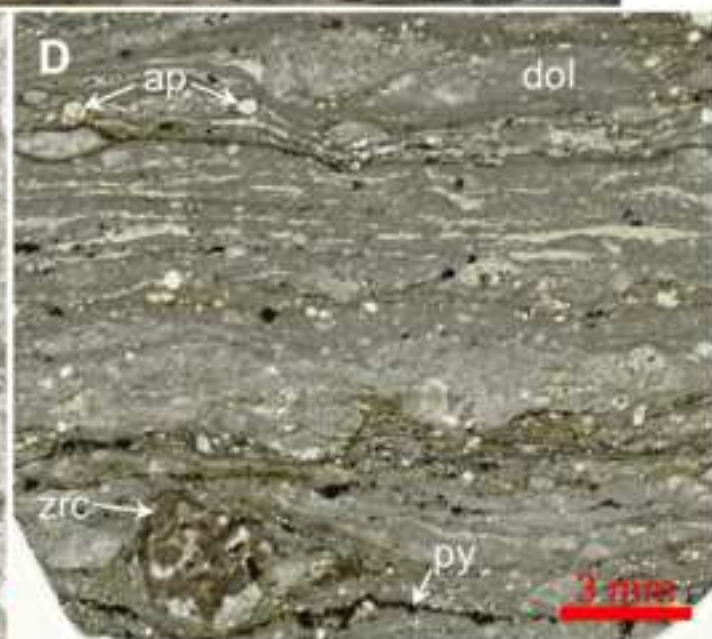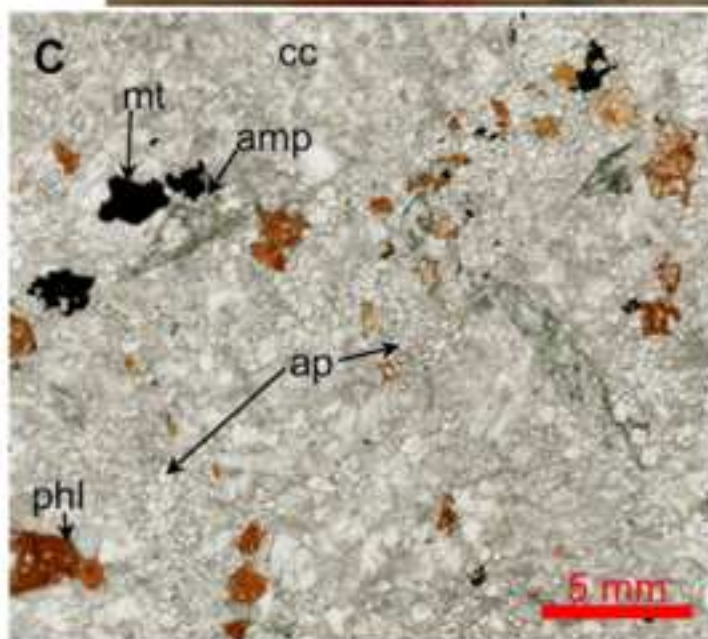
Figure 4
Click here to download high resolution image

Figure 5
Click here to download high resolution image
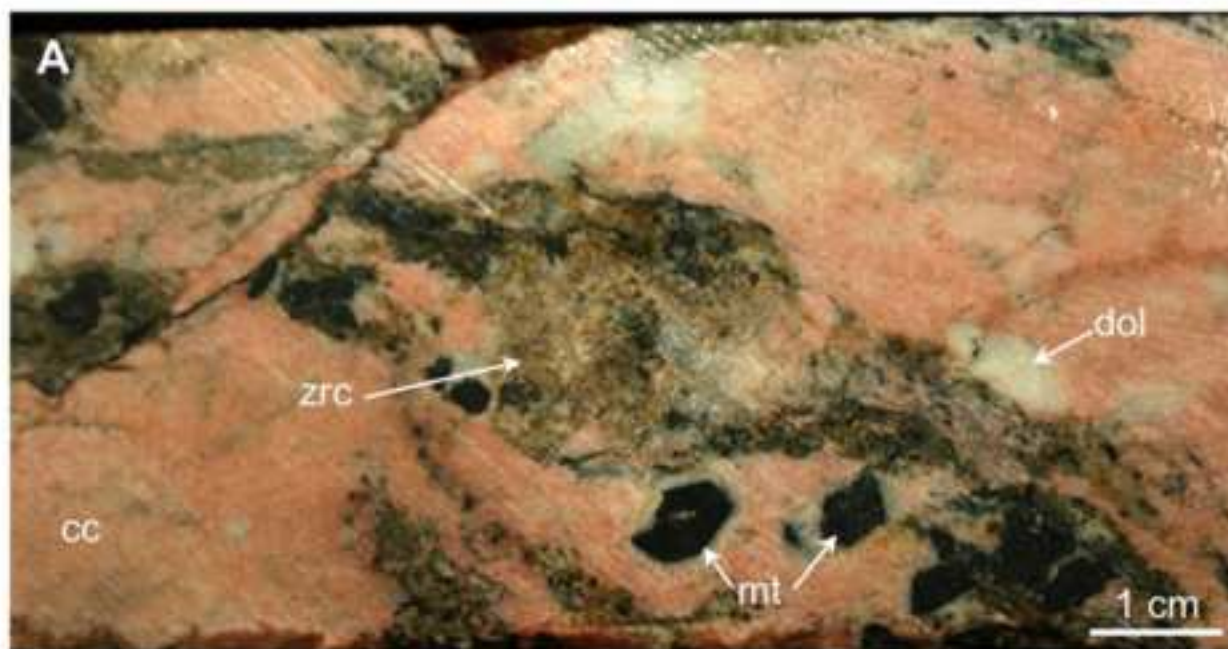
Figure 6
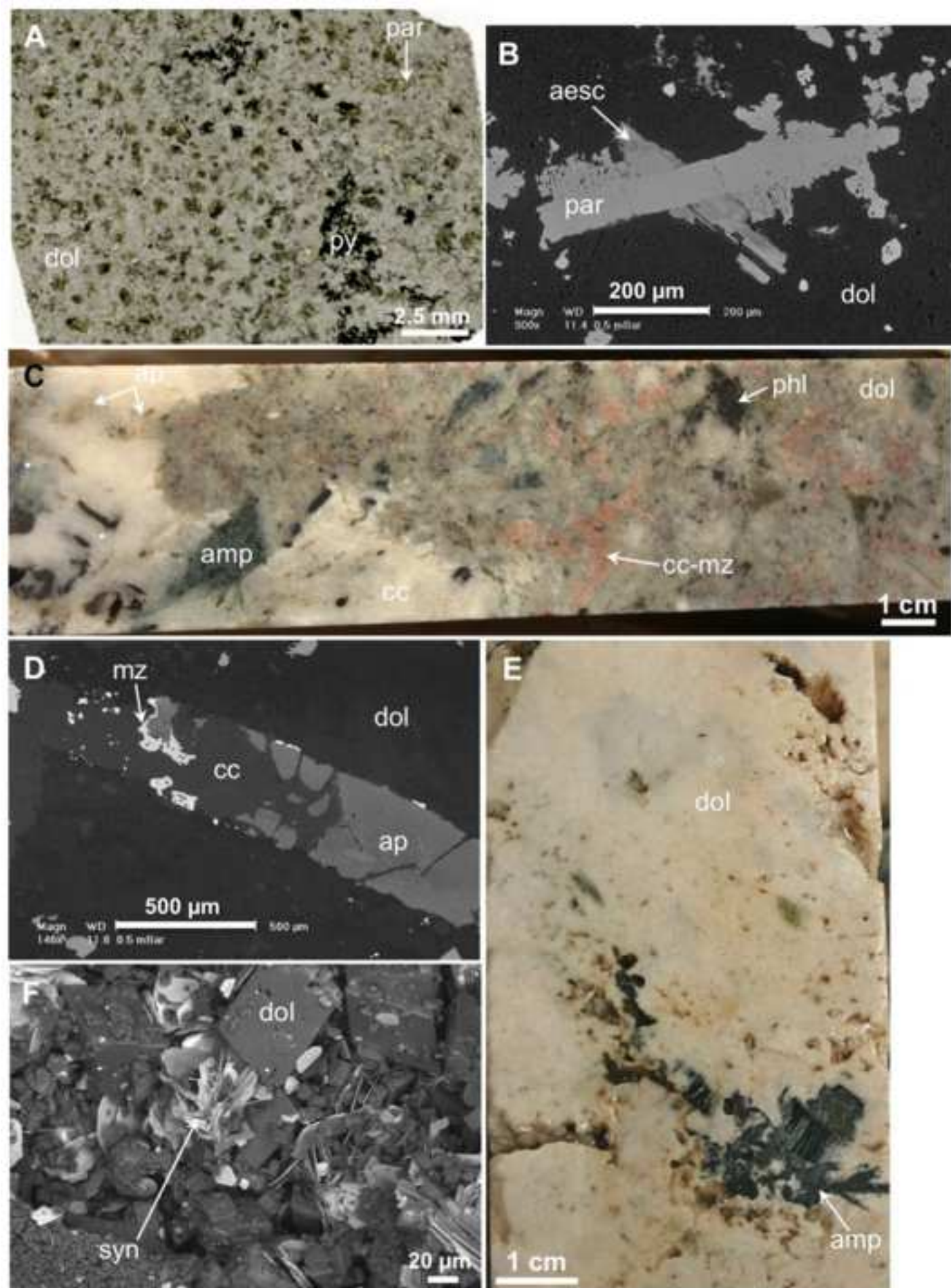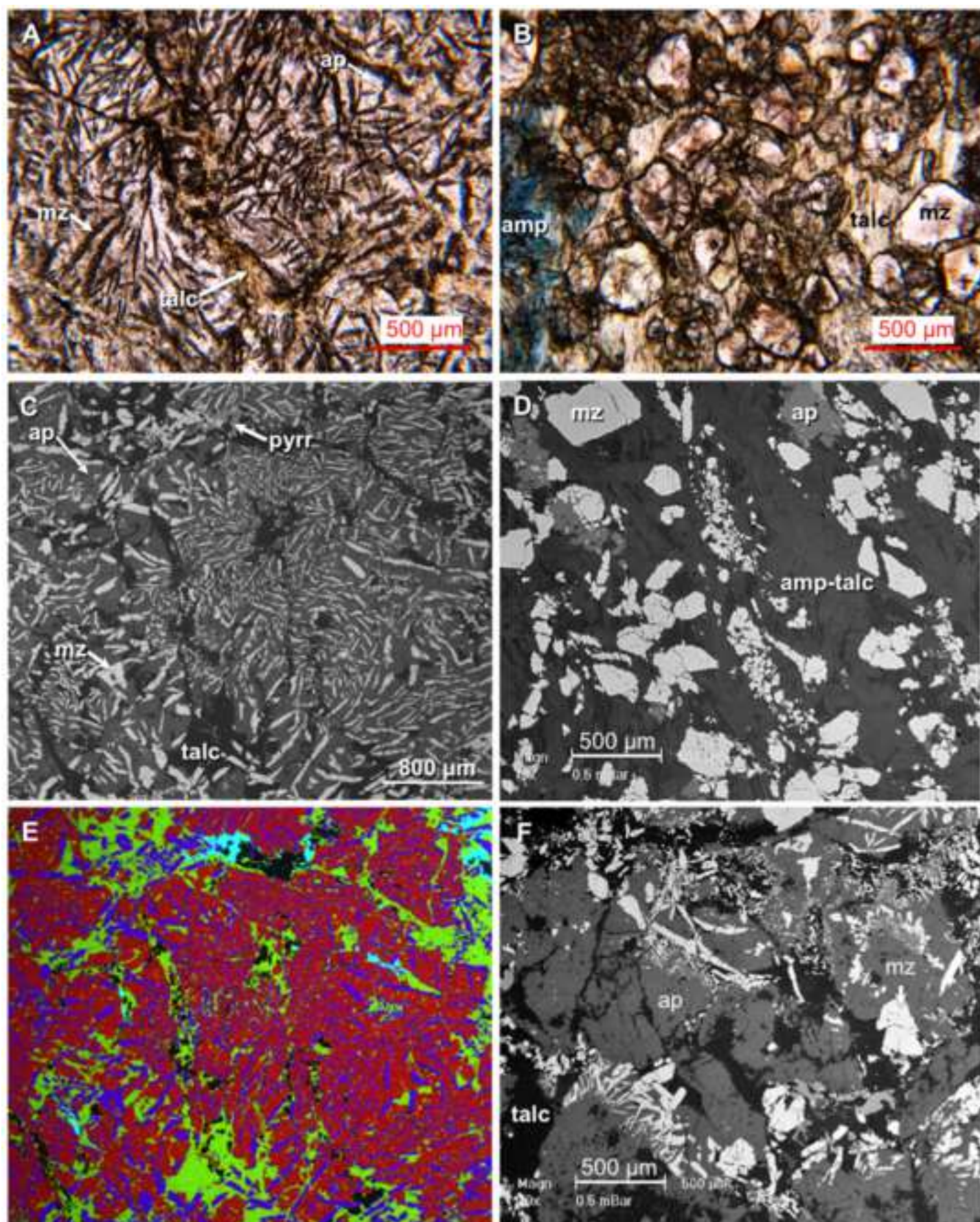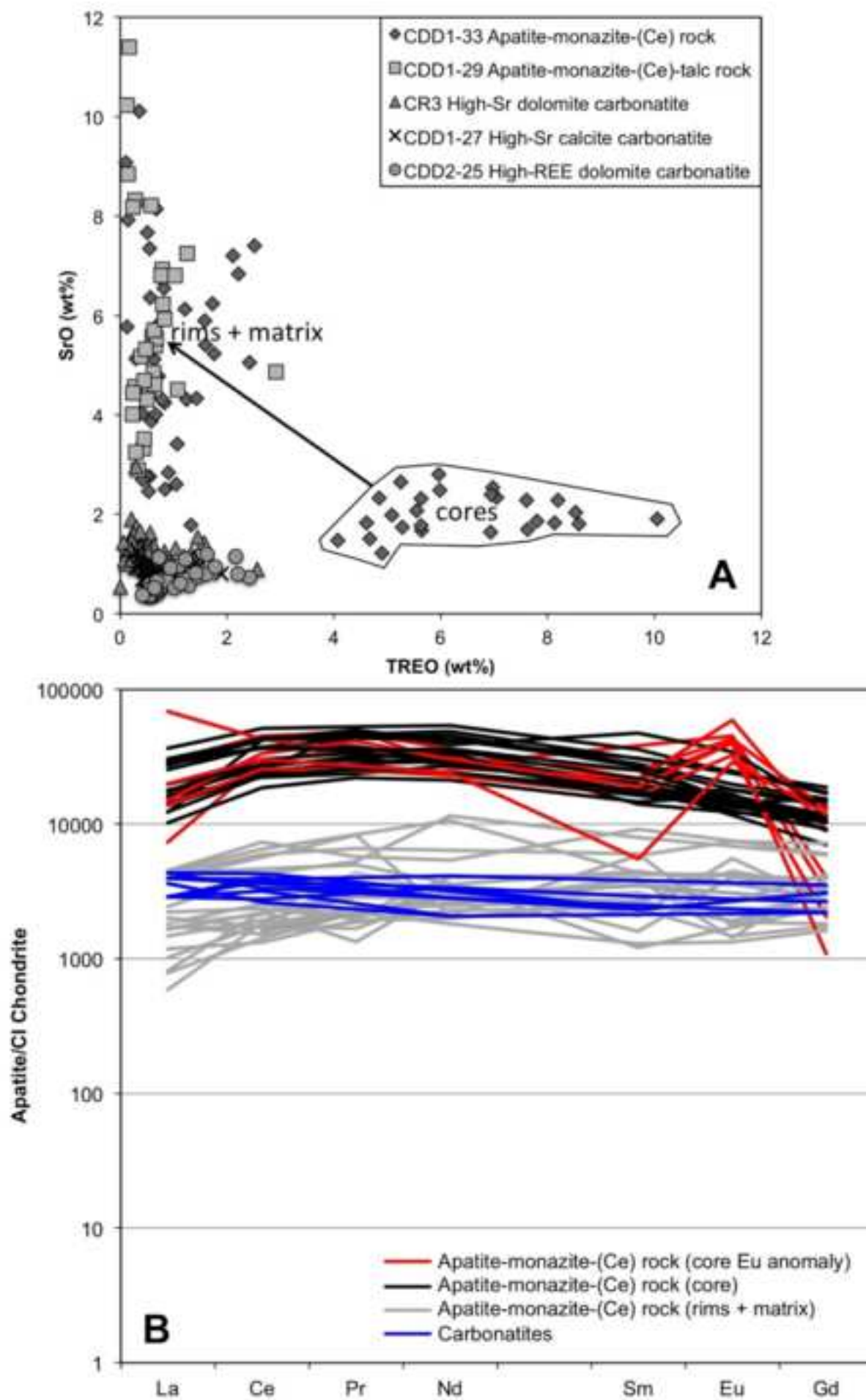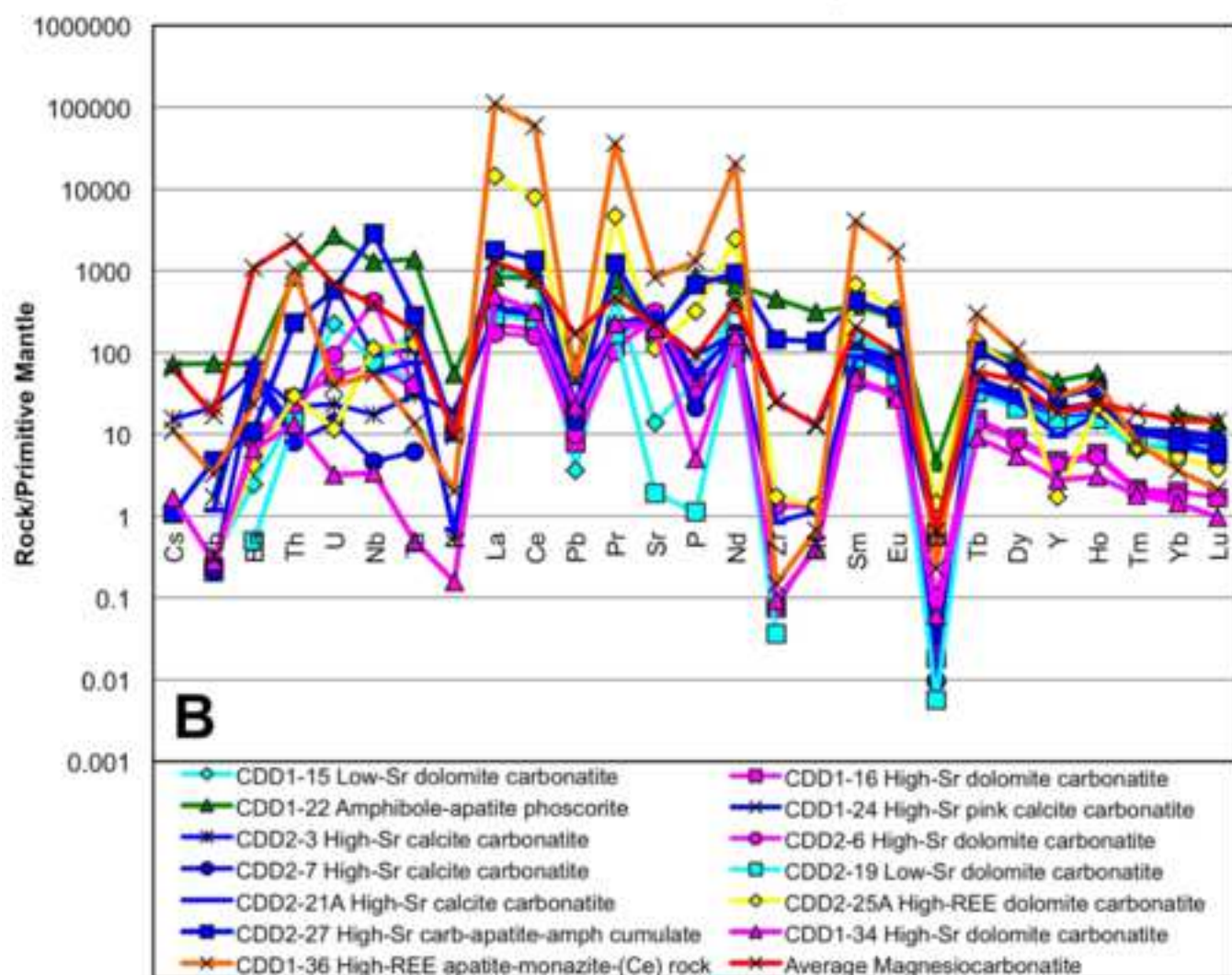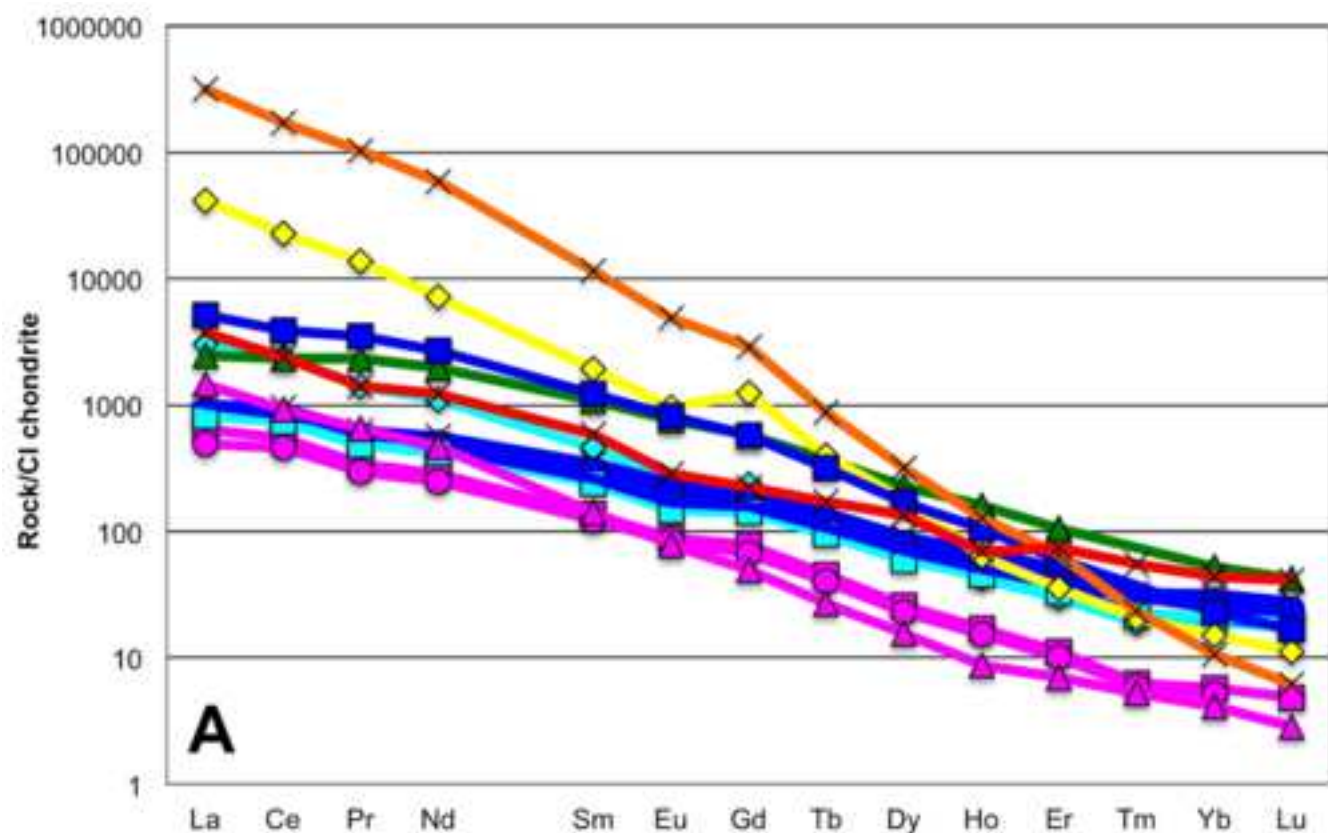Click here to download high resolution image

Ap-mz rock

Ap vein

dol

2.5 mm

Figure 7
Click here to download high resolution image

Figure 8
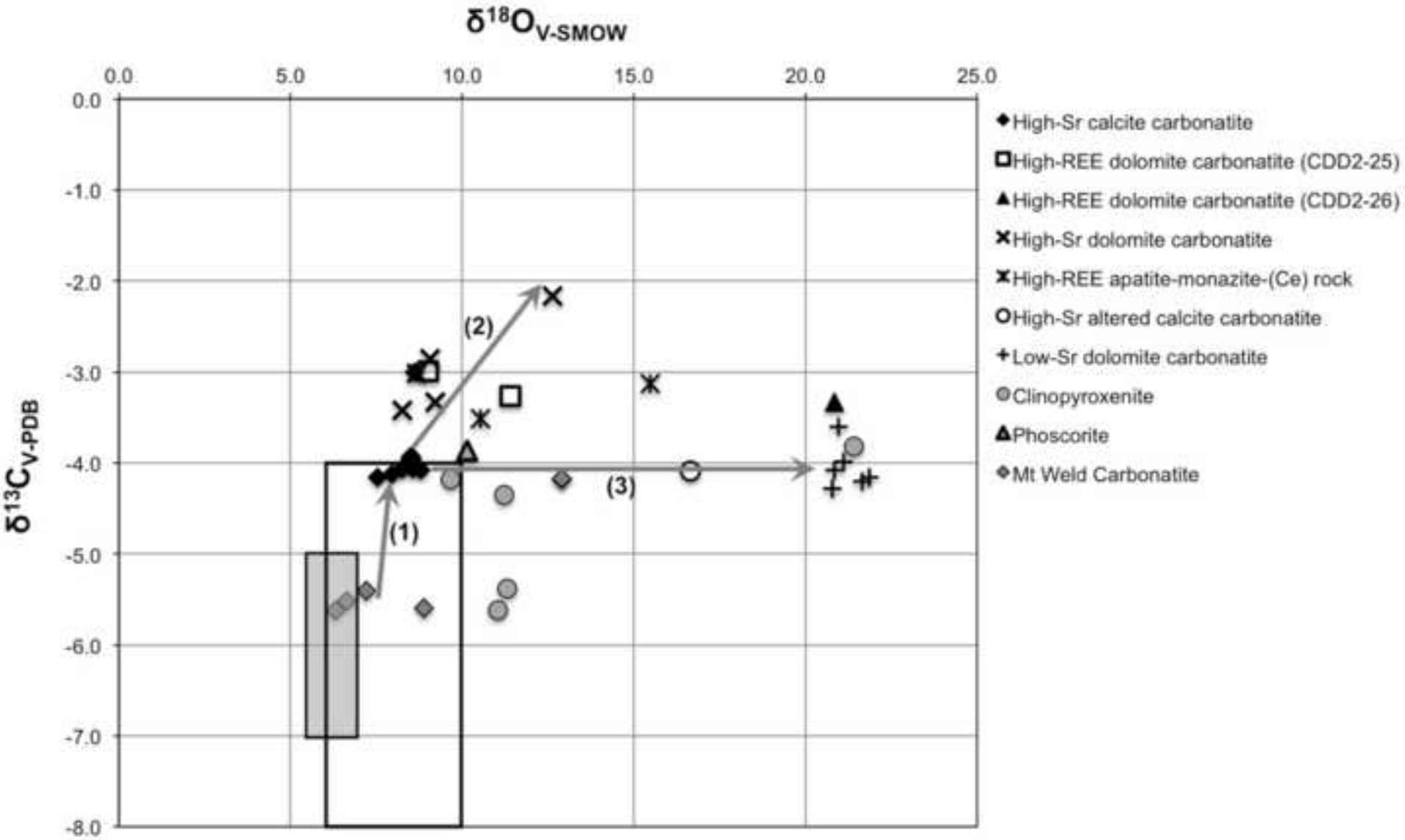
Figure 9

Figure 10

Figure 11
Click here to download high resolution image
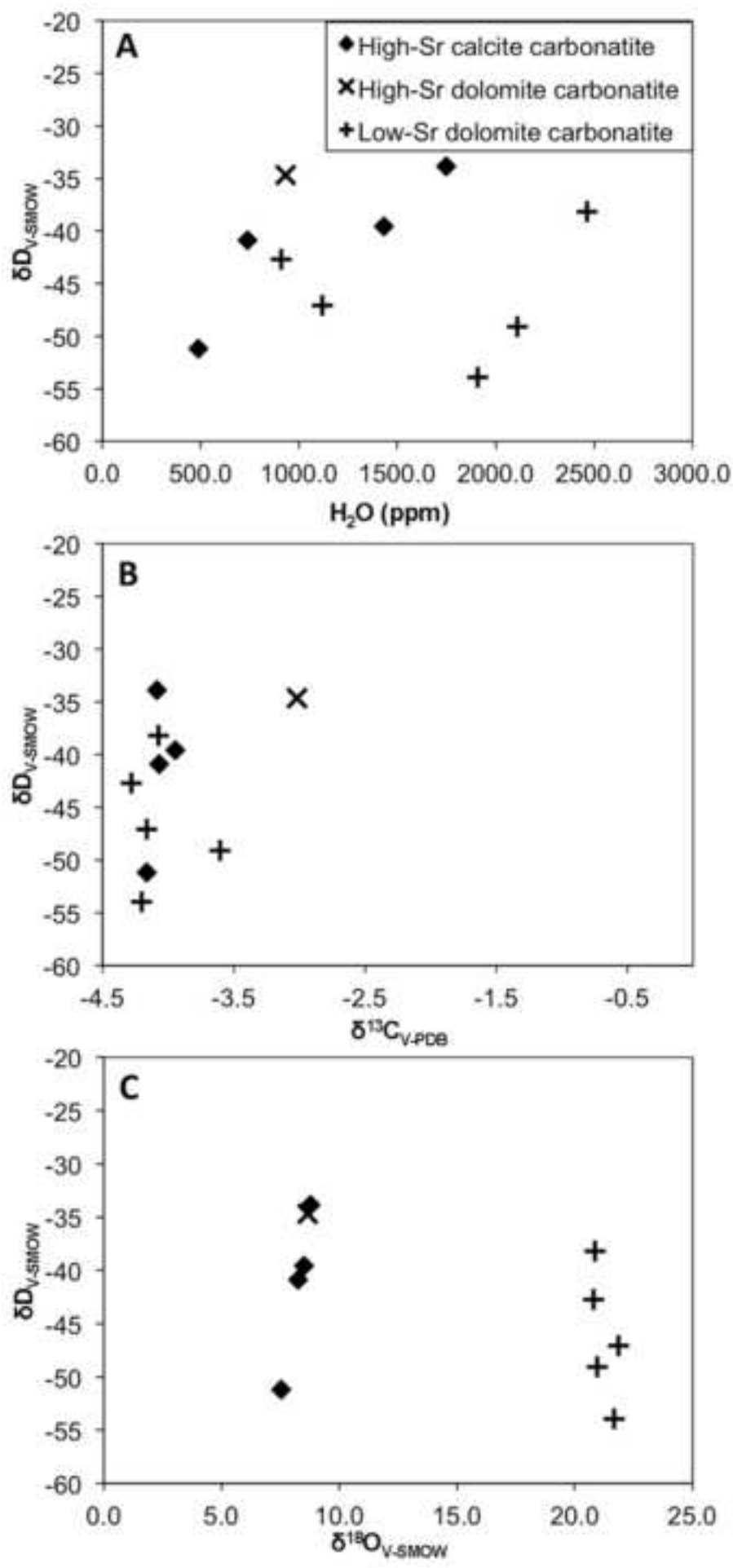
Figure 12
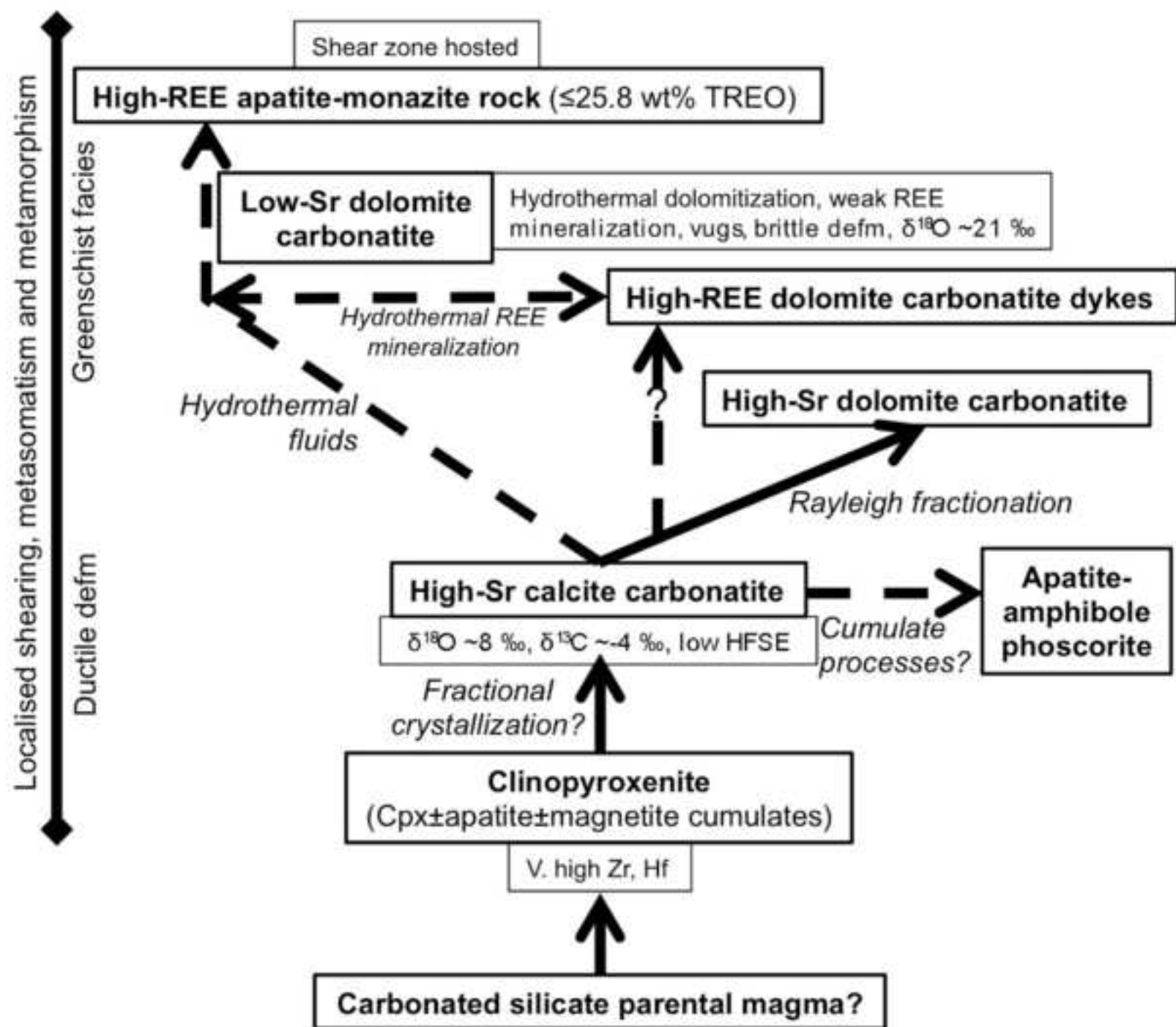
Table 1

Table 1 Mineralogy of the carbonatites and associated rocks from the Cummins Range Carbonatite Complex.

Rock type	Texture	Mineralogy
Clinopyroxenite	Mesocumulate. Medium–coarse-grained.	Phlogopite, diopside, apatite, magnetite, ilmenite, richterite, calcite, dolomite, actinolite (replacing diopside). Pyrrhotite, pyrite, chalcopyrite, galena, sphalerite. Titanite, zirconolite, calzirtite, perovskite (partially–completely replaced by ilmenite, lucasite?, kassite, titanite), baddeleyite, nioboaeschynite-(Ce), monazite-(Ce), allanite-(Ce), zircon, barite.
Phoscorite–series apatite-rich rocks	Cumulate. Medium–coarse-grained, massive to banded and foliated metasomatised rocks.	Apatite, phlogopite, magnetite, richterite–magnesioriebeckite, dolomite, calcite, ilmenite. Pyrite, chalcopyrite, pyrrhotite, sphalerite. Zircon, pyrochlore, nioboaeschynite-(Ce), barite, fluorite.
High-Sr calcite carbonatite	White–light grey to pink. Massive to foliated. Bands of cumulate-textured apatite-phlog-amph-magnetite.	Calcite (≤5 mm), apatite (≤30%; ≤1.5 cm), magnetite (≤30%; ≤3 cm), ilmenite, phlogopite (≤1 cm), amphibole (≤5%; ≤1.3 cm; metasomatic), dolomite (≤5 mm). Pyrrhotite, pyrite, chalcopyrite, sphalerite, galena. Zircon, pyrochlore (≤5%, generally ≤1%; ≤10 mm), nioboaeschynite-(Ce), parisite-(Ce), synchysite-(Ce), barite, chevkinite-(Ce), fergusonite, zirconolite, thorianite?
High-Sr dolomite carbonatite	Massive, white, weakly–moderately fractured dolomite carbonatite.	Dolomite, calcite, strontianite, apatite (≤5%; ≤1.5 mm; crystal clusters ≤1 cm), pyrite (≤1%), pyrrhotite, chalcopyrite, pyrochlore, ilmenite, monazite-(Ce) (≤1%), parisite-(Ce), synchysite-(Ce), Ca-REE-Ba-Sr carbonates (burbankite or carbocernaite?)
High-REE dolomite carbonatite (1)	Massive, medium-grained grey dolomite carbonatite.	Dolomite, parisite-(Ce) (~15–20%; ≤3 mm), pyrite (≤0.6 mm), monazite-(Ce), aeschynite-(Ce) (≤0.8 mm), galena.
High-REE dolomite carbonatite (2)	Massive grey dolomite carbonatite. Pink calcite-monazite-(Ce) replacement textures after apatite.	Dolomite, calcite, apatite, phlogopite, magnetite, monazite-(Ce), parisite-(Ce), synchysite-(Ce), apatite, fergusonite, strontianite, Ca-REE-Ba-Sr carbonates (burbankite or carbocernaite?)
Low-Sr dolomite carbonatite	White–grey foliated to massive with vugs.	Dolomite (≤2 cm), calcite, apatite, magnetite, phlogopite, amphibole, quartz. Pyrite, marcasite, chalcopyrite, sphalerite. Monazite-(Ce), parisite-(Ce), synchysite-(Ce), nioboaeschynite-(Ce), zircon, baddeleyite, pyrochlore, ferrocolumbite.
High-REE apatite-monazite-(Ce) rock	Complex intergrown apatite-monazite-(Ce) texture. Massive to foliated. Interval includes foliated monazite-(Ce)-talc rocks.	Apatite, monazite-(Ce), talc, amphibole, dolomite. Pyrrhotite, pyrite, chalcopyrite (≤5% sulfide mineralization along fractures).

Table 2

Table 2 Representative analyses of apatite from the CRCC.

	Apatite-monazite-(Ce) rock					Carbonatites		
Sample No.	CDD1-33	CDD1-33	CDD1-33	CDD1-33	CDD1-29	CR3	CDD2-25	CDD1-27
Analysis No.	Area 3-1 A13	Area 3-3 A2	Area 3-2 A8	Area 3-2 A9	Area 4 A10	Area 1 A2	A1-4	A6
(wt%)	core	core	core	rim	matrix		core	
Na_2O	n.a.	n.a.	n.a.	n.a.	n.a.	0.22	0.17	0.23
MgO	n.a.	n.a.	n.a.	n.a.	n.a.	0.17	-	-
Al_2O_3	-	-	0.08	0.01	-	-	-	-
SiO_2	-	0.01	-	-	-	0.05	0.28	-
P_2O_5	38.96	39.00	38.94	40.18	38.21	41.00	42.22	43.31
CaO	48.54	50.08	46.32	50.80	47.00	55.18	54.32	52.19
MnO	-	-	-	0.02	0.02	-	-	-
FeO	0.03	0.05	0.02	0.03	0.15	-	-	-
SrO	2.07	1.22	2.04	5.83	11.39	0.94	0.43	1.15
Y_2O_3	0.30	0.31	0.27	0.02	-	0.02	0.02	-
La_2O_3	0.20	0.38	1.90	0.05	0.01	0.14	0.13	0.23
Ce_2O_3	2.07	1.85	3.10	0.16	0.05	0.38	0.28	0.63
Pr_2O_3	0.41	0.27	0.37	0.03	-	0.05	0.05	0.11
Nd_2O_3	1.39	1.23	1.65	0.19	-	0.22	0.14	0.27
Sm_2O_3	0.38	0.28	0.43	0.03	-	-	-	-
Eu_2O_3	0.38	0.21	0.28	0.03	0.01	-	-	-
Gd_2O_3	0.20	0.05	0.29	0.08	-	0.05	0.04	0.06
ThO_2	-	0.02	-	0.01	-	-	-	-
UO_2	0.01	0.01	-	-	-	-	-	-
SO_3	-	-	-	0.03	0.03	-	0.04	-
Cl	-	-	-	0.01	-	-	-	-
F	3.74	3.38	3.61	3.92	3.49	3.65	4.21	4.42
F,Cl=O	-1.57	-1.43	-1.52	-1.65	-1.47	-1.54	-1.77	-1.86
Total	97.10	96.94	97.79	99.77	98.90	100.53	100.56	100.74
Structural formulae calculated to 26 (O,OH,F,Cl)								
Na	n.a.	n.a.	n.a.	n.a.	n.a.	0.072	0.056	0.075
Mg	n.a.	n.a.	n.a.	n.a.	n.a.	0.043	-	-
Al	-	-	0.016	0.001	-	-	-	-
Si	-	0.002	-	-	-	0.008	0.047	-
P	5.650	5.657	5.648	5.828	5.542	5.847	6.021	6.177
Ca	8.909	9.192	8.501	9.325	8.627	9.959	9.804	9.420
Mn	-	-	-	0.002	0.003	-	-	-
Fe	0.005	0.006	0.003	0.004	0.022	-	-	-
Sr	0.206	0.121	0.202	0.579	1.132	0.092	0.042	0.112
Y	0.027	0.029	0.024	0.002	-	0.002	0.002	0.000
La	0.013	0.024	0.120	0.003	0.001	0.009	0.008	0.014
Ce	0.130	0.116	0.195	0.010	0.003	0.023	0.017	0.039
Pr	0.026	0.017	0.023	0.002	-	0.003	0.003	0.007
Nd	0.085	0.075	0.101	0.012	-	0.013	0.008	0.016
Sm	0.022	0.017	0.026	0.002	-	-	-	-
Eu	0.022	0.012	0.016	0.002	0.000	-	-	-
Gd	0.012	0.003	0.017	0.004	-	0.003	0.002	0.003
Th	-	0.001	-	0.000	-	-	-	-
U	0.000	0.000	-	-	-	-	-	-
S	-	-	-	0.004	0.004	-	0.005	-
Cl	0.000	0.001	-	0.003	-	-	-	-
F	2.025	1.833	1.957	2.125	1.892	1.944	2.243	2.355
A-site	9.456	9.613	9.229	9.946	9.788	10.219	9.943	9.687
B-site	5.650	5.659	5.664	5.833	5.546	5.856	6.069	6.177

(- = below detection limits; n.a. = not analysed)

Table 3-6

Table 3 Representative whole-rock geochemistry of carbonatites and associated apatite-rich rocks from the CRCC.

Sample No.	CDD1-16	CDD1-22	CDD2-19	CDD2-21A	CDD2-25A	CDD2-27	CDD1-34	CDD1-36
Depth	150.82 – 151.03 m	251.13 – 251.22 m	370 – 370.15 m	399.78 – 399.95 m	397.45 – 397.59 m	400.5 – 400.68 m	263.75 – 263.85 m	269.75 m
	High-Sr dolomite carbonatite	Amphibole-apatite phoscorite	Low-Sr dolomite carbonatite	High-Sr calcite carbonatite	High-REE dolomite-calcite carbonatite	High-Sr carbonatite-apatite-amph cumulate	High-Sr dolomite carbonatite	High-REE apatite-monazite-(Ce) rock
(wt%)								
SiO_2	0.023	17.79	<0.01	0.29	0.292	8.27	3.49	8.55
TiO_2	0.012	0.975	0.008	0.136	0.305	0.131	0.013	0.049
Al_2O_3	<0.01	2.00	<0.01	0.031	<0.01	0.108	0.095	0.207
Fe_2O_3	0.67	1.56	0.36	0.56	2.32	1.84	1.70	0.890
FeO	3.84	2.98	1.95	0.76	4.60	2.62	18.9	1.10
MnO	0.793	0.168	0.272	0.183	0.822	0.501	0.683	0.116
MgO	19.0	9.03	21.3	1.41	12.0	11.7	12.7	4.01
CaO	30.9	31.5	31.1	55.4	33.9	33.8	21.2	20.9
Na_2O	0.082	1.04	0.061	0.034	0.126	1.05	0.167	0.352
K_2O	0.006	1.72	0.004	0.029	0.009	0.329	0.005	0.062
P_2O_5	0.92	17.05	0.035	1.25	7.28	13.4	0.099	26.1
SrO	0.601	0.415	0.005	0.689	0.270	0.454	0.484	2.00
TREO	0.085	0.440	0.125	0.138	3.43	0.671	0.142	25.8
SO_3	0.443	0.187	0.277	0.038	0.012	0.036	19.8	0.352
LOI	44.0	10.3	46.3	41.4	34.8	24.4	18.9	3.71
F	0.111	2.02	0.040	0.512	0.720	1.39	<0.01	1.22
Cl (ppm)	197	37	448	173	239	65	246	59
Total	101.5	99.2	101.8	102.9	100.9	100.7	98.1	95.5

Table 4 Trace-element geochemistry of carbonatites and associated apatite-rich rocks from the CRCC (samples CDD1-22, CDD2-27, CDD1-34, CDD1-36 analysed at Geoscience Australia and ANU).

Sample No.	CDD1-15	CDD1-16	CDD1-22	CDD1-24	CDD2-3	CDD2-6	CDD2-7	CDD2-19	CDD2-21A	CDD2-25A	CDD2-27	CDD1-34	CDD1-36
Depth	133.7 – 133.95 m Low-Sr dol carb	150.82 – 151.03 m High-Sr dol carb	251.13 – 251.22 m Amph-apatite phoscorite	288.95 – 289.2 m High-Sr calcite carb	82.25 – 82.4 m High-Sr calcite carb	113.9 – 114 m High-Sr dol carb	128.15 – 128.3 m High-Sr calcite carb	370 – 370.15 m Low-Sr dol carb	399.78 – 399.95 m High-Sr calcite carb	397.45 – 397.59 m High-REE dol-calcite carb	400.5 – 400.68 m High-Sr carb-apatite-amph cumulate	263.75 – 263.85 m High-Sr dol carb	269.75 m High-REE apatite-monazite-(Ce) rock
(ppm)													
Li	1.35	1.35	n.a.	5.74	6.88	0.885	0.61	0.274	1.47	1.73	n.a.	n.a.	n.a.
Be	0.284	< 0.100	5.95	0.242	0.307	< 0.100	0.479	< 0.100	< 0.100	0.254	2.95	0.3	1.70
B	< 0.100	5.91	n.a.	5.34	1.24	1.79	13.2	6.84	17.7	11.9	n.a.	n.a.	n.a.
V	3.59	1.29	77.2	0.949	29.8	1.87	0.773	< 0.100	14.9	37.1	34.3	4.0	4.0
Cr	2.33	0.563	24.9	4.01	0.475	0.549	0.617	3.59	0.8	5.47	13.8	22	77
Co	8.32	4.41	12	5.73	7.7	4.8	4.45	4.36	3.86	7.14	8.18	150	22
Ni	1.1	1.31	16	7.31	2.25	< 0.100	4.93	2.05	4.73	< 0.100	12.2	20	24
Cu	37	7.76	127	56.4	10.6	1.8	2.52	< 0.100	14.4	9.58	73.9	1890	28
Zn	5.01	20.1	101	9.92	9.29	28.5	2.94	0.6	7.1	36.1	33.7	44	79
Ga	33.1	5.42	22.2	10.7	14.4	5.14	9.41	8.07	6.38	32.6	20.1	4.0	25.0
Ge	3.84	0.961	1.6	1.99	1.9	0.933	1.83	1.55	1.24	2.89	1.56	0.2	1.7
As	7.88	4.79	3.5	4.14	1.84	1.33	7.05	2.33	17.3	8.12	2.85	1.5	11.0
Se	4.94	2.31	n.a.	6.76	5.52	2.64	6.55	4.84	3.92	2.42	n.a.	n.a.	n.a.
Rb	0.182	0.127	44.6	1.03	12.7	0.133	0.132	< 0.100	0.708	0.168	2.88	0.17	2.0
Sr	282	5080	3507	6060	4800	6310	5060	38.5	5830	2280	3843	4090	16897
Y	51.4	20.7	194	90.3	70.2	19.1	84.8	67	42	7.46	124	12	126
Zr	< 0.100	0.816	4879	279	0.871	14	< 0.100	0.395	8.92	18.5	1544	1	1.6
Nb	47.9	42	764	55.2	10.4	254	2.82	41.7	34.1	67.3	1719	1.92	25
Mo	0.337	0.233	0.33	< 0.100	< 0.100	< 0.100	< 0.100	0.121	0.233	0.187	0.141	1.36	0.23
Ag	n.a.	n.a.	1.59	n.a.	n.a.	n.a.	n.a.	n.a.	n.a.	n.a.	0.328	1.3	0.2
Cd	< 0.100	0.355	1.50	0.339	0.186	0.793	0.25	< 0.100	0.202	0.379	0.862	0.40	0.20
In	< 0.100	0.128	n.a.	0.131	< 0.100	0.241	< 0.100	< 0.100	< 0.100	0.25	n.a.	n.a.	n.a.
Sn	0.165	0.154	3.2	< 0.100	0.289	0.208	< 0.100	0.614	0.203	0.562	3.01	1.5	0.6
Sb	< 0.100	< 0.100	0.08	< 0.100	< 0.100	< 0.100	< 0.100	0.355	< 0.100	< 0.100	0.106	1	4

Table 4 Trace-element geochemistry of carbonatites and associated apatite-rich rocks from the CRCC (samples CDD1-22, CDD2-27, CDD1-34, CDD1-36 analysed at Geoscience Australia and ANU).

Sample No. (ppm)	CDD1-15	CDD1-16	CDD1-22	CDD1-24	CDD2-3	CDD2-6	CDD2-7	CDD2-19	CDD2-21A	CDD2-25A	CDD2-27	CDD1-34	CDD1-36
Cs	< 0.100	< 0.100	1.29	< 0.100	0.279	< 0.100	< 0.100	< 0.100	< 0.100	< 0.100	0.019	0.03	0.2
Ba	16.3	62	490	419	397	57	325	3.32	509	28.4	73.3	44	158
La	717	152	580	239	201	117	210	195	240	9860	1216	345	75020
Ce	1490	338	1440	586	500	284	510	457	515	14200	2408	567	106220
Pr	131	31.8	216	58.7	51.6	27.6	51.7	44.7	61.5	1280	327	61	9650
Nd	508	130	895	260	227	113	230	193	209	3280	1233	213	26904
Sm	68.5	20.3	161	51.3	43.5	18.4	45.4	35.5	38.8	288	184	21	1735
Eu	13.6	4.98	42.9	13.6	11.4	4.71	11.9	8.3	9.41	53.9	45.7	4.4	276
Gd	46.8	15.5	115	40.4	32.5	13.1	34.9	28.2	31.3	244	113	9.85	571
Tb	4.29	1.62	13.25	5.03	3.95	1.42	4.44	3.38	3.78	14.3	11.3	0.96	31
Dy	16.1	6.4	55.7	22.4	16.8	5.65	19.7	14.6	17.4	43.6	41.7	3.84	78
Ho	2.32	0.926	8.82	3.81	2.75	0.835	3.35	2.47	2.78	3.49	5.78	0.48	7.03
Er	4.75	1.79	16.8	8.17	5.8	1.62	7.28	5.35	6.07	5.71	9.68	1.11	10.5
Tm	0.466	0.155	n.a.	0.811	0.545	0.145	0.718	0.535	0.746	0.508	n.a.	0.13	0.58
Yb	3.05	0.922	8.33	5.09	3.32	0.817	4.47	3.42	3.9	2.41	3.65	0.66	1.68
Lu	0.42	0.119	1.03	0.682	0.429	< 0.100	0.594	0.459	0.56	0.276	0.410	0.07	0.15
Hf	< 0.100	< 0.100	93	3.81	0.136	0.388	< 0.100	< 0.100	0.345	0.4	41.1	0.127	0.20
Ta	1.74	1.44	55	4.37	1.24	1.6	0.246	7.39	3.03	5.06	11.3	0.02	0.54
W	19.4	17.5	9	13.7	42.7	26	26.7	23.9	21.4	35.3	20.4	58	32
Tl	< 0.100	< 0.100	n.a.	< 0.100	< 0.100	< 0.100	< 0.100	< 0.100	< 0.100	< 0.100	n.a.	n.a.	n.a.
Pb	0.664	1.44	13.1	7.92	2.99	1.87	2.66	< 0.100	3.40	3.57	4.00	4.00	7.25
Bi	< 0.100	< 0.100	0.065	< 0.100	< 0.100	< 0.100	< 0.100	< 0.100	< 0.100	< 0.100	0.073	0.02	<0.02
Th	1.58	2.25	70	0.965	1.8	1.52	0.669	1.2	0.666	2.42	19.4	1.1	85
U	4.97	1.1	60	15	0.505	2.02	0.3	< 0.100	< 0.100	0.253	12.7	0.07	0.86
Sc	14	10.3	13.1	21.1	7.12	12.4	14.7	8.2	3.42	0.187	56.7	20.0	45.0
Zr/Hf	-	-	52.5	73.2	6.40	36.1	-	-	25.9	46.3	37.6	7.87	8.00
Nb/Ta	27.5	29.2	13.9	12.6	8.39	159	11.5	5.64	11.3	13.3	152	96.0	46.3
Th/U	0.318	2.05	1.17	0.064	3.56	0.752	2.23	-	-	9.57	1.53	15.7	98.8
Ga/Ge	8.62	5.64	13.6	5.38	7.58	5.51	5.14	5.21	5.15	11.3	12.9	17.4	14.7
Y/Ho	22.2	22.4	22.0	23.7	25.5	22.9	25.3	27.1	15.1	2.14	21.5	25.0	17.9

(n.a. – not analysed)

Table 5 Stable C and O isotope compositions (in ‰ relative to V-PDB and V-SMOW, respectively) of carbonatites and associated rocks from the CRCC.

Sample No.	Hole No.	Depth (m)	Rock type	$\delta^{13}C$	$\delta^{18}O$
CR3	CDD1	151.8–151.94	High-Sr dol carb	-3.4	8.3
CR10	CDD1	324–324.1	High-Sr pink cc carb	-4.1	8.6
CR14	CDD1	401.65–401.75	High-Sr cc carb	-4.1	8.0
CDD2-3	CDD2	82.25–82.4	High-Sr cc carb	-4.1	8.3
CDD2-6	CDD2	113.9–114	High-Sr dol carb	-3.0	8.7
CDD2-7	CDD2	128.15–128.3	High-Sr cc carb	-4.1	8.8
CDD2-9	CDD2	178.05–178.15	High-Sr cc carb	-4.0	8.5
CDD2-22	CDD2	401.9–402	High-Sr cc carb	-4.2	7.5
NRC-35	NRC035	92–93	Dol carb	-3.3	9.2
NRC-58	NRC058	97–98	High-Sr cc carb	-3.0	8.6
CR7	CDD1	235.84–235.94	Dol carb	-2.2	12.6
CR12	CDD1	375–375.1	High-Sr cc carb	-4.1	16.7
CR13	CDD1	386–386.1	Low-Sr dol carb	-4.0	21.1
CDD2-1	CDD2	69.5–69.65	Low-Sr dol carb	-4.1	20.9
CDD2-10	CDD2	199–199.15	Low-Sr dol carb	-4.2	21.7
CDD2-12	CDD2	225.65–225.8	Low-Sr dol carb	-3.6	21.0
CDD2-18	CDD2	328.78–328.94	Low-Sr dol carb	-4.2	21.9
CDD2-19	CDD2	370–370.15	Low-Sr dol carb	-4.3	20.8
CDD2-25 cc	CDD2	397.35–397.45	High-REE dol carb	-3.3	11.4
CDD2-25 dol	CDD2	397.35–397.45	High-REE dol carb	-3.0	9.0
CDD2-26	CDD2	225.2	High-REE dol carb	-3.3	20.8
CDD1-31	CDD1	269.5	High-REE ap-mz rock	-3.1	15.5
CDD1-37A	CDD1	270.3	High-REE ap-mz rock	-3.5	10.5
CDD1-37B	CDD1	270.3	Dol carb	-2.9	9.1
CDD2-5	CDD2	92.9–93	Ap-phl phoscorite	-3.9	10.1
CDD2-11	CDD2	220.6–220.7	Clinopyroxenite	-5.4	11.3
CDD2-14	CDD2	250.85–251	Clinopyroxenite	-5.6	11.1
CDD2-17A	CDD2	293.6–293.79	Clinopyroxenite	-4.4	11.2
CDD2-23	CDD2	231.12–231.44	Clinopyroxenite	-4.2	9.7
CDD2-24	CDD2	309.85–310.06	Clinopyroxenite	-3.8	21.4
Mt Weld-88A			Mt Weld carbonatite	-4.2	12.9
Mt Weld-88B			Mt Weld carbonatite	-4.2	12.9
Mt Weld-1			Mt Weld carbonatite	-5.6	8.9
Mt Weld-2			Mt Weld carbonatite	-5.4	7.2
Mt Weld-87A			Mt Weld carbonatite	-5.6	6.3
Mt Weld-87B			Mt Weld carbonatite	-5.5	6.6

Table 6 H_2O-contents ("H_2O", in ppm) and stable hydrogen isotope compositions of fluid inclusion-hosted H_2O (in ‰ relative to V-SMOW), as well as bulk carbonate C and O isotope compositions (in ‰ relative to V-PDB and V-SMOW, respectively) for ten carbonate samples from the Cummins Range carbonatites.

Sample No.	Hole No.	Depth (m)	Rock type	H_2O	δD	$δ^{13}C$	$δ^{18}O$
CDD2-1	CDD2	69.5–69.65	Low-Sr dol carb	2466	-38	-4.1	20.9
CDD2-3	CDD2	82.25–82.4	High-Sr cc carb	737	-41	-4.1	8.3
CDD2-6	CDD2	113.9–114	High-Sr dol carb	932	-35	-3.0	8.7
CDD2-7	CDD2	128.15–128.3	High-Sr cc carb	1749	-34	-4.1	8.8
CDD2-9	CDD2	178.05–178.15	High-Sr cc carb	1431	-40	-4.0	8.5
CDD2-10	CDD2	199–199.15	Low-Sr dol carb	1909	-54	-4.2	21.7
CDD2-12	CDD2	225.65–225.8	Low-Sr dol carb	2110	-49	-3.6	21.0
CDD2-18	CDD2	328.78–328.94	Low-Sr dol carb	1119	-47	-4.2	21.9
CDD2-19	CDD2	370–370.15	Low-Sr dol carb	907	-43	-4.3	20.8
CDD2-22	CDD2	401.9–402	High-Sr cc carb	489	-51	-4.2	7.5

Supplementary Material

Click here to download Supplementary Material: Supplementary data Appendix 1.xlsx